



Available online at www.sciencedirect.com

ScienceDirect

Mathematics and Computers in Simulation 182 (2021) 116–142

MATHEMATICS
AND
COMPUTERS
IN SIMULATION
IMACS

www.elsevier.com/locate/matcom

Original articles

Accuracy and computational efficiency of dealiasing schemes for the DNS of under resolved flows with strong gradients

Arijit Sinhababu*, Sathyanarayana Ayyalasomayajula

School of Mechanical Sciences, IIT Bhubaneswar, India

Received 13 July 2019; received in revised form 13 March 2020; accepted 23 October 2020

Available online 31 October 2020

Abstract

In this paper, we have studied the effect of residual aliasing error of the second order Runge–Kutta (RK2) based Random Phase Shift Method (RPSM) which shows smoothing effect in the solution of under-resolved flows involving strong gradients. Firstly, we show that RPSM is almost as accurate as the fully dealiased 3/2 Padding scheme but with similar computational cost as the fast 2/3 Truncation scheme. Secondly, we show that RPSM has high accuracy in the case of under-resolved shear layer and Surface Quasi-Geostrophic (SQG) flows. Further, we show that the 2/3 Truncation scheme turns more computationally expensive than 3/2 Padding or RPSM when we try to achieve the same level of accuracy. Filtering based dealiasing schemes are found to be an inappropriate choice for a variety of flow problems because they are prone to unphysical parasitic currents. For the first time error norm based computational efficiency, *i.e.*, high accuracy at the lower computational cost of RPSM scheme is shown. Although some artifacts of dealiasing remain due to Fourier windowing in RPSM, it is found to be numerically stable even in under-resolved conditions at later simulation time. We have validated our numerical results with the analytical ones and also with the previous literature.

© 2020 International Association for Mathematics and Computers in Simulation (IMACS). Published by Elsevier B.V. All rights reserved.

Keywords: Strong gradients; Shear layers; Strong shocks; Dealiasing; Computational efficiency; DNS

1. Introduction

Dealiasing schemes play an important role in accurately simulating flows having strong gradients (*e.g.* flows with shocks, thin shear layers, Surface Quasi-Geostrophic (SQG) flows, etc.). The artifacts and inaccuracies associated with inadequate dealiasing become more acute when the gradients grow in time while the spatial resolution remains fixed. DNS of Navier–Stokes (NS) equations for the simulation of turbulent flows starting from Orszag (1969) [35] to numerous DNS of various canonical turbulent flows of recent times are essentially based on Fourier spectral methods. Although the dealiasing schemes were developed around four decades ago, there are very few studies [1,50] which quantify accuracy and performance of the dealiasing schemes in the presence of strong gradient. The role of aliasing errors and dealiasing is an important aspect of such DNS. In the same study [35], FFTs were also used to solve Poisson's equation for the pressure. In a short communication, Orszag [36] first introduced the 2/3 Truncation dealiasing scheme by filtering the high wavenumber components. The 2/3 Truncation scheme¹ is a

* Correspondence to: IIT Bhubaneswar, Khurda, Odisha 752050, India.

E-mail address: as20@iitbbs.ac.in (A. Sinhababu).

¹ Sometimes called the 2/3 rule.

frequently used dealiasing scheme that has lower computational cost and adequate accuracy. Kaneda et al. [29] also studied DNS of homogeneous isotropic turbulence for the Lagrangian and Eulerian two-point velocity correlations in turbulence at moderate Reynolds number using 2/3 rule. 2/3 rule dealiasing scheme is implemented in various problems [3,31,32,39] such as 3D miscible Rayleigh–Taylor turbulence, 3D decaying MHD turbulence on a periodic domain, rotating turbulence and drag reduction phenomenon by polymer additives in wall-bounded turbulent flows. Mortensen et al. [34] have developed a Python based parallel Pseudo-spectral code by employing the 2/3 Truncation dealiasing scheme. Hou et al. [23] used a variant of 2/3 rule called higher order exponential smoothing filter to remove the aliasing errors from the solutions of 3D incompressible Euler equations. Grauer et al. [18] studied the development of singularity of the 3D incompressible Euler equations using adaptive remeshing technique. The resolution issues become crucial in some cases like passive scalar mixing and SQG flows which develop finite time singularity from sufficiently smooth initial conditions. Hybrid resolution strategy [10,17,37] was adopted to obtain a computationally efficient and accurate solutions.

Random phase shift method (RPSM) based RK2 [42,43] and Spherical Truncation dealiasing schemes were adopted in the homogeneous turbulent shear flow turbulence [6,28] and shearless mixing layer [27]. Many other direct numerical simulation studies use the expensive but most accurate 3/2 Padding dealiasing scheme also. A variety of studies [13,20,24,25,46] are based on the 3/2 Padding scheme involving the DNS of isotropic flow, DNS of incompressible plane channel flow, the homogeneous shear flow turbulence, 1D nonlinear Schrodinger equation, DNS of turbulent mixing layer and multi-scale simulation of geophysical turbulence. Iovieno et al. [26] also studied the novel aspect of a parallel procedure for the numerical simulation of the solution of the Navier–Stokes equation through the Fourier–Galerkin Pseudo-Spectral method using 3/2 rule for dealiasing purpose. The aliasing removal procedure was directly inserted into the transposition algorithm and the code was developed for distributed memory computers. A different dealiasing scheme, implicit padding was developed by Roberts et al. [41], a method for calculating dealiased linear convolution sums without the expense of conventional zero paddings or phase shift method. Implicitly dealiased convolutions can be built using the libraries such as FFTW [14,15]. They note that developing a high performance dealiased Pseudo-spectral code for solving the nonlinear partial differential equations has become a relatively less complicated exercise of late. Cai et al. [7] developed a memory saving algorithm for retaining computer memory at the time of solving the homogeneous isotropic turbulence problem. Homann et al. [21] studied the effect of floating-point accuracy and interpolation schemes in the DNS of turbulence.

More recently, Hou et al. [22] computed nearly singular solutions of inviscid Burgers' equation using Pseudo-spectral method. Dealiasing was performed using 2/3 truncation and Higher Order Fourier Smoothing to suppress the unwanted oscillations throughout the whole domain. The effect of aliasing errors is often neglected in low Reynolds number Pseudo-spectral simulations. The aliasing errors may become significant creating both errors as well as instabilities in the simulations at higher Reynold's number and particularly for just-resolved or under-resolved DNS cases. The issue may get compounded if strong shocks or small scale vortical structures formed in mixing layers are present. The effect of dealiasing is important in the shear layer problem where very thin vortical structures are formed. Brown et al. [5] and Minion et al. [33] did not use dealiasing schemes in their studies. Unphysical spurious vortices are formed in under-resolved shear layers if suitable dealiasing scheme is not chosen properly. Strong shocks are characterized by large amplitude variations in flow properties occurring over short distances and in terms of Fourier modes, high spatial frequencies and large Fourier mode amplitudes of the physical quantities. Implementation of an appropriate dealiasing scheme is important to maintain the accuracy and correct small scale behavior of the DNS, particularly where shocks and small scale vortical structures are involved and in other cases where accurate capturing of small scale behavior is critical. 2/3 Truncation scheme and other variants of the same are widely used to dealias the Pseudo-spectral solutions of most DNS currently. This scheme shows poor convergence at the time of the singularity development, i.e., when strong shocks are present in the flow, and exhibits large amplitude, high-frequency erroneous Gibbs oscillation phenomena. The relative performance of the various dealiasing schemes has also not been studied extensively, especially in the presence of strong gradients. An appropriate flow has to be chosen where a high degree of nonlinearity exists along with the presence of strong shocks, strong gradients or small scale mixing to highlight the effect of dealiasing. The one-dimensional viscous Burgers' equation with appropriately chosen viscosity is one such test case. The effect of dealiasing is distinctly captured in this simple equation because it can create an evolving strong shock after a finite time and evolves a broadband spectrum. The other test cases (2D shear layer and SQG flows) taken up here have features such as small scale mixing, vortex roll-up and highly energetic steep gradients interacting with each other.

In the current study, we also document for the first time the detailed computational performance benefits and accuracy of the RPSM along with its derivation and some key properties. We compare two popular dealiasing schemes: 2/3 Truncation, 3/2 Padding with RPSM. RPSM is found to have the nearly same accuracy as the computationally expensive 3/2 dealiasing scheme having significantly lesser computational complexity, almost the same as the popular 2/3 Truncation scheme for a variety of flows with strong gradients.

This paper is organized as follows: In Section 2, Fourier-Galerkin formulations of one-dimensional viscous Burgers' equation, two-dimensional double shear layer via Euler equations and SQG flows are discussed briefly. A short introduction to aliasing error and the implementation of different dealiasing schemes are shown in Section 3. In Section 3, we also present the detailed derivation of the RPSM scheme as well as the present properties of the scheme. In Section 4, the time-integration scheme is briefly summarized. In Section 5, the computational performance of the various dealiasing schemes is investigated and reported. In Section 6, detailed computational results for (i) an under-resolved and just-resolved DNS of the viscous Burgers' equation including velocity field, velocity derivative, error norms; (ii) 2D double shear layer based on Euler equations and (iii) SQG flow equations are discussed.

2. Test cases

2.1. Strong shock in viscous Burgers' equation

The 1D Viscous Burgers' Equation (VBE) is

$$\frac{\partial u}{\partial t} + u \frac{\partial u}{\partial x} = v \frac{\partial^2 u}{\partial x^2} \quad (1)$$

in which the nonlinear steepening ($u \frac{\partial u}{\partial x}$) and diffusion ($v \frac{\partial^2 u}{\partial x^2}$) compete. The viscous diffusion term has the effect of smoothing out shock discontinuities that form at early time while also acting as an energy sink by reducing shock amplitude. A sinusoidal initial condition for the velocity field is taken

$$u(x, 0) = -\sin(x); \quad x \in [-\pi, \pi] \quad (2)$$

with periodic boundary conditions being imposed. Using the Fourier truncation operator, \mathcal{P}_N , the velocity field u and the n th derivative of the velocity field are expressed as the superposition of Fourier modes evaluated at N discrete collocation points, x_j [8,30].

$$\mathcal{P}_N \{u(x_j)\} = \sum_{\kappa=-\frac{N}{2}+1}^{\frac{N}{2}} \hat{u}_\kappa e^{i\kappa x_j}; \quad \frac{d^n}{dx^n} \{\mathcal{P}_N u(x_j)\} = \sum_{\kappa=-\frac{N}{2}+1}^{\frac{N}{2}} (i\kappa)^n \hat{u}_\kappa e^{i\kappa x_j} \quad (3)$$

where the spatial index $j = 0, 1, 2, \dots, N - 1$ and the discrete wave number $\kappa = -\frac{N}{2} + 1, -\frac{N}{2} + 2, \dots, 0, \dots, \frac{N}{2} - 1, \frac{N}{2}$.

Using the orthogonality conditions, the Discrete Fourier Transform (DFT) in the forward direction is given by:

$$\hat{u}_\kappa = \frac{1}{N} \sum_{j=0}^{N-1} u_j e^{-i\kappa x_j} \quad (4)$$

The nonlinear term is calculated using the Pseudo-spectral or Collocation formulation where the nonlinear product is evaluated in physical space as

$$\mathcal{NL}_j = u_j \left(\frac{\partial u}{\partial x} \right)_j; \quad j = 0, 1, 2, \dots, N - 1. \quad (5)$$

The nonlinear term in the spectral space $\widehat{\mathcal{NL}}_\kappa$ is calculated efficiently from \mathcal{NL}_j by using forward Fast Fourier Transform (FFT). N real values of the nonlinear term in physical space transform to $(\frac{N}{2} + 1)$ complex Fourier amplitudes using optimized real to complex FFTs. Here, in this study we use the open source FFTW3 [15] libraries, to perform the Fourier transforms. The 1D VBE can be expressed in spectral space as

$$\frac{d\hat{u}_\kappa}{dt} + \widehat{\mathcal{NL}}_\kappa = -v\kappa^2 \hat{u}_\kappa \quad (6)$$

and can be computationally evaluated with RK2 scheme as discussed later in Section 4 to perform accurate DNS.

2.2. Unstable double shear layer in Euler equations

The two dimensional incompressible Euler equations along with the continuity equation are

$$\frac{\partial u_i}{\partial t} + u_j \frac{\partial u_i}{\partial x_j} = - \frac{\partial p}{\partial x_i} \quad (7a)$$

$$\frac{\partial u_i}{\partial x_i} = 0 \quad (7b)$$

where u_i ($i = 1, 2$ denotes space co-ordinates x, y , respectively) are the velocity components, p is the density-normalized pressure and t is time. The computation is performed on a square, $x, y \in [0, 2\pi] \times [0, 2\pi]$ and periodicity is assumed in both x and y directions with spatial period 2π . The velocity field is expanded in the two dimensional discrete Fourier space as

$$\mathcal{P}_N \{u(x_p, y_q)\} = \sum_{|\kappa_1| \leq \frac{N_1}{2}} \sum_{|\kappa_2| \leq \frac{N_2}{2}} \hat{u}(\kappa_1, \kappa_2) e^{i(\kappa_1 x_p + \kappa_2 y_q)} \quad (8)$$

where the spatial indices $p = 0, 1, \dots, N_1 - 1; q = 0, 1, \dots, N_2 - 1$ and the 2D wave numbers $\kappa_1 = -\frac{N_1}{2} + 1, \dots, 0, \dots, \frac{N_1}{2}; \kappa_2 = -\frac{N_2}{2} + 1, \dots, 0, \dots, \frac{N_2}{2}$.

The initial condition taken for the unstable shear layer is

$$u(x, y) = \begin{cases} \tanh\{(y - \pi/2)/\rho\}, & y \leq \pi \\ \tanh\{(3\pi/2 - y)/\rho\}, & y > \pi \end{cases} \quad (9a)$$

$$v(x, y) = \delta \sin(x) \quad (9b)$$

Here, we have used the classical double shear layer initial conditions summarized in the Eqs. (9a) and (9b) (see Refs. [2,5,19,49,51] and [33]) with a sinusoidal velocity perturbation in the y direction. We simulate for shear layer parameter, $\rho = \pi/15$ and $\rho = \pi/150$ with perturbation amplitude $\delta = 0.05$. With $\rho = \pi/15$ the shear layer is termed thick and with $\rho = \pi/150$ it is termed thin, relatively. For this type of problem, a dealiasing scheme's performance depends on its ability to resolve the small scales accurately during the roll up process. A scheme's inherent filtering may inadvertently smooth these causing inconsistencies in the flow physics. Using the Fourier representation of velocity (8) and the Poisson equation for pressure, the 2D Euler equations can be transformed into spectral space as

$$\frac{d\hat{u}_i}{dt} + \mathcal{P}_{ij} \widehat{\mathcal{NL}}_j = 0 \quad (10)$$

where the projection tensor $\mathcal{P}_{ij} = \left[\delta_{ij} - \frac{\kappa_i \kappa_j}{\kappa^2} \right]$ [40] and the nonlinear term in the two dimensional Fourier domain is $\widehat{\mathcal{NL}}_j = \mathcal{F}_{\bar{k}} \left\{ u_i \frac{\partial u_j}{\partial x_i} \right\}$. Again, the two equations (10) are advanced in time using RK2 scheme as summarized in Section 4.

2.3. Strong fronts in the SQG flows

The governing equations of the SQG Flows [11,12] are given as

$$\frac{\partial \theta}{\partial t} + u \frac{\partial \theta}{\partial x} + v \frac{\partial \theta}{\partial y} = 0 \quad (11)$$

Eq. (11) is expressed in the Fourier domain as

$$\frac{\partial \widehat{\theta}}{\partial t} + \mathcal{F}_{(\kappa_1, \kappa_2)} \left(u \frac{\partial \theta}{\partial x} \right) + \mathcal{F}_{(\kappa_1, \kappa_2)} \left(v \frac{\partial \theta}{\partial y} \right) = 0 \quad (12)$$

The dealiasing schemes: RK2 based RPSM, circular truncation (CT) and 3/2 Padding are employed to compute the nonlinear terms $(u \frac{\partial \theta}{\partial x})$ and $(v \frac{\partial \theta}{\partial y})$. We use similar initial condition [11,12] to study the evolution of potential temperature field as

$$\theta(x, y, 0) = \cos(x) \cos(2y) + \sin(2x) \sin(2y) \quad (13)$$

Here, the velocity components u and v are coupled as follows: $u = \mathcal{F}^{-1} \left[\frac{-ik_2}{\kappa} \hat{\theta} \right]$, $v = \mathcal{F}^{-1} \left[\frac{ik_1}{\kappa} \hat{\theta} \right]$ where $\kappa^2 = \kappa_1^2 + \kappa_2^2$. The above set of equations is marched forward in time using RK2 temporal scheme as discussed below in Section 4.

3. Aliasing errors and dealiasing schemes

3.1. Aliasing errors

In Pseudo-spectral based DNS of flows aliasing errors develop at the time of calculating the nonlinear terms in discrete Fourier space. A high-order nonlinear term can be expressed in discrete Fourier space as

$$\mathcal{P}_N \{u(x_j)\} \mathcal{P}_N \left\{ \frac{\partial^n u}{\partial x^n} \right\}_{x_j} = \sum_{p=-\frac{N}{2}+1}^{\frac{N}{2}} \sum_{q=-\frac{N}{2}+1}^{\frac{N}{2}} (\iota q)^n \hat{u}_p \hat{u}_q e^{i(p+q)x_j} \quad (14)$$

where $x_j = (j - 1) \frac{2\pi}{N}$; ($j = 1, 2, \dots, N$) are the collocation points. Aliasing error occurs when the summation of wave numbers $(p + q)$ lies outside the range of $\left[\frac{2\pi}{L} \left(-\frac{N}{2} + 1 \right), \frac{2\pi}{L} \left(\frac{N}{2} \right) \right]$ when gradients are sharp. For example the nonlinear term $(u \frac{\partial u}{\partial x})$ in spectral domain for 1D Burgers' equation can be split into two parts [9,30] and can be expressed as

$$\widehat{\mathcal{NL}}_\kappa = \left(\iota \sum_{p+q=\kappa} \kappa \hat{u}_p \hat{u}_q \right) + \left(\iota \sum_{p+q=\kappa \pm N} \kappa \hat{u}_p \hat{u}_q \right), \quad (15)$$

or

$$\widehat{\mathcal{NL}}_\kappa = \widehat{S}(\kappa|p, q) + \widehat{\mathcal{A}}(\kappa \pm N|p, q), \quad (16)$$

where $\widehat{S}(\kappa|p, q)$ and $\widehat{\mathcal{A}}(\kappa \pm N|p, q)$ stands for actual convolution and aliasing error term, respectively. The aliasing error, $\widehat{\mathcal{A}}(\kappa \pm N|p, q)$, becomes significant at the time of development of strong shocks inside the domain [1,22], SQG flows and thin shear structures [2,49]. The aliasing error occurs when the wave number interactions $(p + q)$ in nonlinear term exceeds the Nyquist Sampling limit. For example in the VBE, a single frequency signal becomes broad-band with occurrence of high-frequency components that corresponds to the nearly singular solution, the Nyquist Sampling criterion is exceeded (particularly for the case of low viscosity, $\nu \leq 0.001$) in finite time ($T \approx 0.5$)[1].² Similar broadening of spectra occurs whenever strong gradients evolve due to the nonlinear convective action in other flow problems. Due to this aliasing error, the simulation blows up without the usage of suitable dealiasing schemes or filtering. In the case of SQG flows, the aliasing error shows up, as a noisy potential temperature field and for the thin shear layer evolution via Euler equations, it produces spurious vorticity and non-physical flow instability.

3.2. Propagation of aliasing errors in the random phase shift method

Random Phase Shift Method (RPSM) [9,43] is an elegant way of dealiasing using the sub-steps of explicit RK2 scheme which provides high accuracy without significantly increasing the computational cost of performing the pseudo-spectral operation. In this scheme, the nonlinear term is calculated introducing a random shift of $\Delta_1 = \Delta$ in the first stage of RK2 and introducing another shift $\Delta_2 = (\Delta + \frac{\pi}{N})$ in the second stage [9,43]. Here, Δ is a uniformly distributed random number in the range $(0, \frac{2\pi}{N})$ and it is updated for each complete iteration of the RK2 time stepping scheme. The nonlinear terms in spectral space over the shifted grids are calculated for RK2 sub-steps k_1 and k_2 as

$$\widehat{\mathcal{NL}}|_{k_1} = \mathcal{F}_\kappa \left[\mathcal{F}_\kappa^{-1} \{ \hat{u} e^{i\kappa \Delta_1} \} \mathcal{F}_\kappa^{-1} \{ i\kappa \hat{u} e^{i\kappa \Delta_1} \} \right] e^{-i\kappa \Delta_1} \quad (17)$$

$$\widehat{\mathcal{NL}}|_{k_2} = \mathcal{F}_\kappa \left[\mathcal{F}_\kappa^{-1} \{ (\hat{u} + \Delta t \cdot k_1) e^{i\kappa \Delta_2} \} \mathcal{F}_\kappa^{-1} \{ i\kappa (\hat{u} + \Delta t \cdot k_1) e^{i\kappa \Delta_2} \} \right] e^{-i\kappa \Delta_2} \quad (18)$$

² The values of T and ν mentioned relate exclusively to the initial condition chosen in the paper for the VBE.

The RK2 time integration scheme is discussed in Section 4. The sub-steps k_1, k_2 of RK2 with RPSM become

$$k_1 = \Delta t [\widehat{\mathcal{N}\mathcal{L}}|_{k_1} + \widehat{\mathcal{V}}\{\hat{u}(\kappa, t^n)\}] \quad (19)$$

$$k_2 = \Delta t [\widehat{\mathcal{N}\mathcal{L}}|_{k_2} + \widehat{\mathcal{V}}\{\hat{u}(\kappa, t^n) + k_1, t_n + \Delta t\}] \quad (20)$$

$\widehat{\mathcal{N}\mathcal{L}}\{\cdot\}, \widehat{\mathcal{V}}\{\cdot\}$ denote the nonlinear and viscous terms in spectral space, respectively. With $\Delta_1 = \Delta$ and $\Delta_2 = (\Delta + \frac{\pi}{N})$ it can be shown that the dominant effect of the aliasing of the order of Δt vanishes and the next higher order aliasing error terms of $O(\Delta t^2)$ remains but due to the uncorrelated random aspect of the error it remains bounded. We shall show through numerical tests that the residual error of RPSM implemented with RK2 is found to be nearly the same as a fully dealiased scheme (here 3/2 Padding), without loss of higher wave-number information as in 2/3 Truncation (or circular truncation) or external filtering (see Section 6.2). The uniform random distribution Δ results not just in the aliasing errors being uncorrelated between the iteration but also limits the growth of truncation errors as the simulation proceeds. Some oscillations (similar to 3/2 Padding) are created in Random Phase Shift Method (RPSM) due to the spectral leakage effect of shifted window in the physical space especially at low values (high Re) of ν (see Section 6.2).

3.2.1. Residual aliasing error in RK2 based RPSM

Following is the derivation of the aliasing error in the RK2 based RPSM formulation, here we illustrate using the 1D VBE. Writing the RHS of the governing equation $\mathcal{L}(\hat{u}, t^n)$ in the 1st sub-step of RK2 as $\mathcal{L}(\hat{u})^{(n,0)}$, we obtain

$$\mathcal{L}(\hat{u})^{(n,0)} = [\widehat{\mathcal{V}}_1^{(n,0)} - \{\widehat{\mathcal{S}}_1^{(n,0)} + \widehat{\mathcal{A}}_1^{(n,0)}\}] \quad (21)$$

where

$$\widehat{\mathcal{V}}_1^{(n,0)} = -\kappa^2 \hat{u}^{(n,0)} \quad (22a)$$

$$\widehat{\mathcal{S}}_1^{(n,0)} = \sum_{m+p=\kappa} \hat{u}_m^{(n,0)} \hat{v}_p^{(n,0)} \quad (22b)$$

$$\widehat{\mathcal{A}}_1^{(n,0)} = e^{\pm i N \Delta_1} \left\{ \sum_{m+p=\kappa \pm N} \hat{u}_m^{(n,0)} \hat{v}_p^{(n,0)} \right\} \quad (22c)$$

Here

$$\hat{v}_p^{(n,0)} = (\iota p) \hat{u}_p^{(n,0)}$$

and \mathcal{V} indicates the viscous term, \mathcal{S} the actual nonlinear term computed using the Pseudo-spectral method and \mathcal{A} the aliasing term containing the phase shifts.

In a similar way for 2nd sub-step of RK2, $\mathcal{L}(\hat{u}, t^n)$ denoted by $\mathcal{L}(\hat{u})^{(n,1)}$ where

$$\mathcal{L}(\hat{u})^{(n,1)} = [\widehat{\mathcal{V}}_2^{(n,1)} - \{\widehat{\mathcal{S}}_2^{(n,1)} + \widehat{\mathcal{A}}_2^{(n,1)}\}] \quad (23)$$

and

$$\widehat{\mathcal{V}}_2^{(n,1)} = -\kappa^2 \hat{u}^{(n,1)} \quad (24a)$$

$$\widehat{\mathcal{S}}_2^{(n,1)} = \sum_{m+p=\kappa} \hat{u}_m^{(n,1)} \hat{v}_p^{(n,1)} \quad (24b)$$

$$\widehat{\mathcal{A}}_2^{(n,1)} = e^{\pm i N \Delta_2} \left\{ \sum_{m+p=\kappa \pm N} \hat{u}_m^{(n,1)} \hat{v}_p^{(n,1)} \right\} \quad (24c)$$

The sub-steps of RK2 are

$$k_1 = \Delta t [\widehat{\mathcal{V}}_1^{(n,0)} - \{\widehat{\mathcal{S}}_1^{(n,0)} + \widehat{\mathcal{A}}_1^{(n,0)}\}] \quad (25a)$$

$$k_2 = \Delta t [\widehat{\mathcal{V}}_2^{(n,1)} - \{\widehat{\mathcal{S}}_2^{(n,1)} + \widehat{\mathcal{A}}_2^{(n,1)}\}] \quad (25b)$$

The aliasing errors $\widehat{\mathcal{A}}_1^{(n,0)}, \widehat{\mathcal{A}}_2^{(n,1)}$ for the two sub-steps of RK2 due to the Pseudo-spectral computation of the nonlinear term can be written using as

$$\widehat{\mathcal{A}}_1^{(n,0)} = \Delta t e^{\pm i N \Delta_1} \left\{ \sum_{m+p=\kappa \pm N} \hat{u}_m^{(n,0)} \hat{v}_p^{(n,0)} \right\} \quad (26a)$$

$$\widehat{\mathcal{A}}_2^{(n,1)} = \Delta t e^{\pm i N \Delta_2} \left\{ \sum_{m+p=\kappa \pm N} \hat{u}_m^{(n,1)} \hat{v}_p^{(n,1)} \right\} \quad (26b)$$

Performing time step update for RK2, we obtain

$$\hat{u}_m^{(n,1)} = \hat{u}_m^{(n,0)} + \left[\widehat{\mathcal{V}}_1^{(n,0)} - \left\{ \widehat{\mathcal{S}}_1^{(n,0)} + \widehat{\mathcal{A}}_1^{(n,0)} \right\} \right] \quad (27a)$$

$$\hat{v}_p^{(n,1)} = \hat{v}_p^{(n,0)} + i p \left[\widehat{\mathcal{V}}_1^{(n,0)} - \left\{ \widehat{\mathcal{S}}_1^{(n,0)} + \widehat{\mathcal{A}}_1^{(n,0)} \right\} \right] \quad (27b)$$

where $i = \sqrt{-1}$. Considering only the contribution of aliasing terms and using Eq. (26b), we obtain

$$\begin{aligned} \mathcal{A}_2^{(n,1)} &= \Delta t e^{\pm i N \Delta_2} \left[\sum_{m+p=\kappa \pm N} \hat{u}_m^{(n,0)} \hat{v}_p^{(n,0)} \right] - \Delta t e^{\pm i N \Delta_2} \\ &\quad \times \left[\Delta t e^{\pm i N \Delta_1} \sum_{m+p=\kappa \pm N} \left\{ \sum_{m+p=\kappa \pm N} \hat{u}_m^{(n,0)} \hat{v}_p^{(n,0)} \right\} \left\{ i p \hat{u}_m^{(n,0)} + \hat{v}_p^{(n,0)} \right\} \right] \\ &\quad - 2 \Delta t e^{\pm i N \Delta_2} \left[\Delta t e^{\pm i N \Delta_1} \sum_{m+p=\kappa \pm N} \left\{ i p \sum_{m+p=\kappa \pm N} \hat{u}_m^{(n,0)} \hat{v}_p^{(n,0)} \right\} \left\{ \widehat{\mathcal{V}}_1^{(n,0)} - \widehat{\mathcal{S}}_1^{(n,0)} \right\} \right] \\ &\quad + \Delta t e^{\pm i N \Delta_2} \left[\Delta t^2 e^{\pm 2 i N \Delta_1} \sum_{m+p=\kappa \pm N} (i p) \left\{ \sum_{m+p=\kappa \pm N} \hat{u}_m^{(n,0)} \hat{v}_p^{(n,0)} \right\}^2 \right] \end{aligned} \quad (28)$$

The residual aliasing errors terms are conveniently written as

$$\mathcal{H}_1 = \sum_{m+p=\kappa \pm N} \left\{ \sum_{m+p=\kappa \pm N} \hat{u}_m^{(n,0)} \hat{v}_p^{(n,0)} \right\} \left\{ i p \hat{u}_m^{(n,0)} + \hat{v}_p^{(n,0)} \right\} \quad (29a)$$

$$\mathcal{H}_2 = \sum_{m+p=\kappa \pm N} \left\{ i p \sum_{m+p=\kappa \pm N} \hat{u}_m^{(n,0)} \hat{v}_p^{(n,0)} \right\} \left\{ \widehat{\mathcal{V}}_1^{(n,0)} - \widehat{\mathcal{S}}_1^{(n,0)} \right\} \quad (29b)$$

$$\mathcal{H}_3 = \sum_{m+p=\kappa \pm N} (i p) \left\{ \sum_{m+p=\kappa \pm N} \hat{u}_m^{(n,0)} \hat{v}_p^{(n,0)} \right\}^2 \quad (29c)$$

Finally

$$\mathcal{A}_2^{(n,1)} = \Delta t e^{\pm i N \Delta_2} \left[\sum_{m+p=\kappa \pm N} \hat{u}_m^{(n,0)} \hat{v}_p^{(n,0)} - \Delta t e^{\pm i N \Delta_1} \mathcal{H}_1 - 2 \Delta t e^{\pm i N \Delta_1} \mathcal{H}_2 + \Delta t^2 e^{\pm 2 i N \Delta_1} \mathcal{H}_3 \right] \quad (30)$$

Neglecting the effect of higher order terms $O(\Delta t^3)$ and beyond, the total contribution of aliasing errors (τ_a) after the final RK2 time-step is

$$\tau_a = (\tau_p + \tau_h) = \left[\frac{\widehat{\mathcal{A}}_1^{(n,0)} + \widehat{\mathcal{A}}_2^{(n,1)}}{2} \right] \quad (31)$$

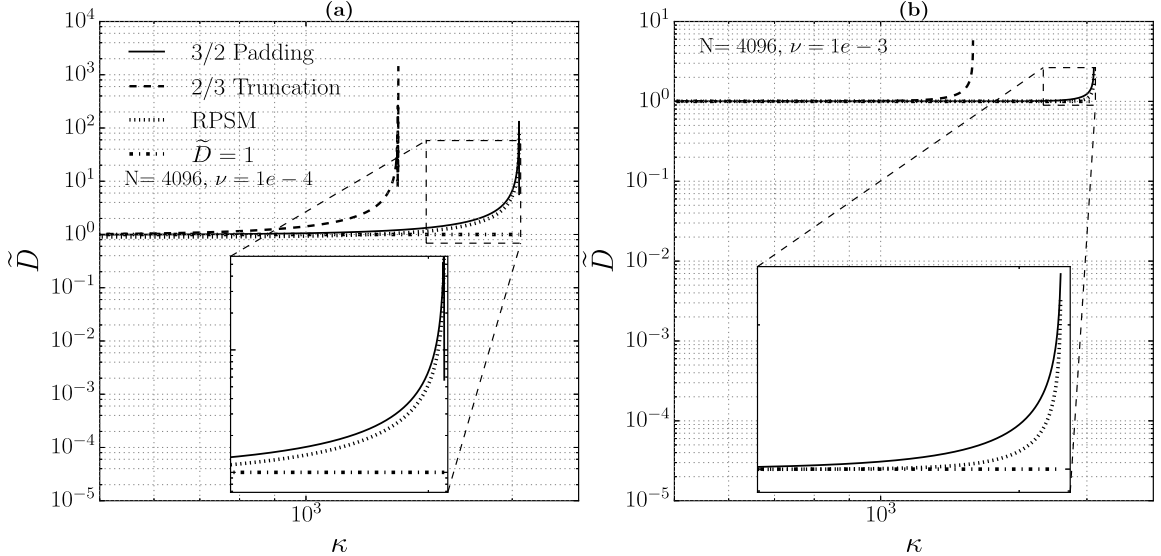


Fig. 1. Damping function $\tilde{D}(\kappa)$ of 1D VBE at $T = 0.5$ (a) for $N = 4096$ & $\nu = 1e-4$; (b) for $N = 4096$ & $\nu = 1e-3$.

The primary and the higher order aliasing error terms are represented as

$$\tau_p = \Delta t \left(\frac{e^{\pm i N \Delta_1} + e^{\pm i N \Delta_2}}{2} \right) \sum_{m+p=\kappa \pm N} \hat{u}_m^{(n,0)} \hat{v}_p^{(n,0)} \quad (32)$$

$$\tau_h = -\Delta t^2 e^{\pm i N (\Delta_1 + \Delta_2)} \left(\frac{\mathcal{H}_1}{2} + \mathcal{H}_2 \right) \quad (33)$$

The primary aliasing term (τ_p) vanishes by choosing the random phase shifts $\Delta_1 = \Delta$ and $\Delta_2 = (\Delta + \frac{\pi}{N})$ [42,43]. Due to the randomization of the higher order aliasing term, τ_h , does not accumulate and remains bounded stabilizing the simulation. We numerically show next that the RPSM has weakly dissipative property.

3.2.2. Effect of residual aliasing error with RPSM scheme

The effect of higher order aliasing error (τ_h) is visualized using the dissipation spectra. Here, the dissipation spectra $D(\kappa)$ [40] for an one dimensional problem is defined as

$$D(\kappa, t) = 2\nu\kappa^2 \hat{u}(\kappa) \hat{u}^*(\kappa); \quad \kappa = -N/2 + 1, \dots, 0, \dots, N/2. \quad (34)$$

We introduce a metric called Damping Function (\tilde{D}) to quantify the dissipative property of a numerical scheme based on the dissipation spectra for a given simulation. It is defined as

$$\tilde{D}(\kappa) = \frac{D(\kappa)}{D_{\text{high-res}}(\kappa)} \quad (35)$$

$D(\kappa)$ is the dissipation spectra of an under-resolved/just-resolved pseudo-spectral simulation. $D_{\text{high-res}}$ is the dissipation spectra of a high resolution simulation. Area under the dissipation spectra computes the energy dissipation. In the case of a well-resolved simulation that uses a spectrally accurate scheme $\tilde{D}(\kappa)$ should be unity throughout the range of resolved wave numbers, κ . In Fig. 1(a) and (b), $\tilde{D}(\kappa)$, as a function of wave number is plotted for $\nu = 1e-4$ and $\nu = 1e-3$, respectively. At the higher viscosity value of $\nu = 1e-3$ both RPSM and 3/2 Padding techniques have identical $\tilde{D}(\kappa)$ and yield normally unity for the entire range of resolved wave number except for the tail end where the windowing effect of both techniques cause small amount of spectral leakage. In contrast, the 2/3 Truncation introduces a larger accumulation due to windowing and also causes large deviation from unity for wave numbers around $\kappa_c (= N/3)$ as well as $\kappa > \kappa_c$, where κ_c is the cut-off frequency.

From Fig. 1, the 2/3 Truncation technique creates anomalous values of heavy dissipation for $\nu = 1e-4$ and under-resolved simulation with $N = 4096$. Both RPSM and 3/2 Padding techniques have identical behavior here too,

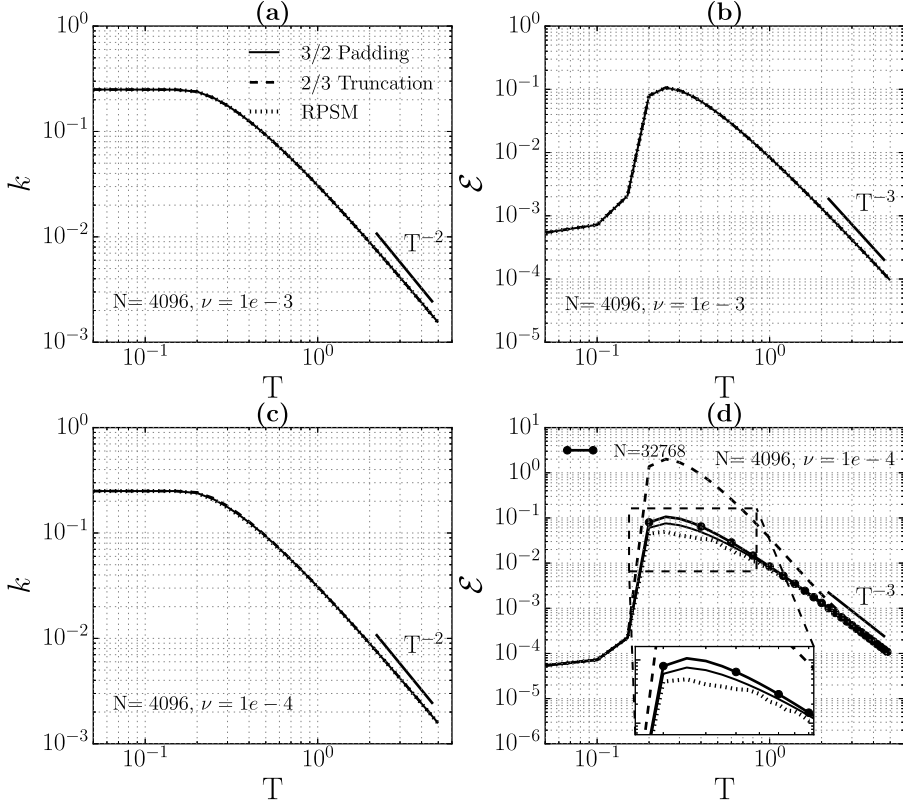


Fig. 2. For $N = 4096$ & $\nu = 1e-3$, (a) kinetic Energy, k ; (b) energy dissipation rate, \mathcal{E} . For $N = 4096$ & $\nu = 1e-4$, (c) kinetic Energy, k (d) energy dissipation rate, \mathcal{E} . Black solid line with bullets (\bullet) in (d) is the High Resolution data ($N = 32768$).

but also show similar anomalous trend of slightly higher damping. From the perspective of the Damping Function we can say that RPSM is equally good when compared to the computationally costly 3/2 Padding in both adequately and under-resolved simulations whereas the 2/3 Truncation is inaccurate even for adequately resolved simulations. From Fig. 2(d), reduced value in decay of dissipation due to the effect of accumulation of higher order aliasing error terms is observed for the RPSM scheme at $T = 0.5$. Fig. 2(d) also shows a over estimation of dissipation rate during the formation of strong shock at $\nu = 1e-4$ for 2/3 Truncation.

3.3. 3/2 Padding

The 3/2 Padding scheme [9,13,30] removes the aliasing error by introducing extra zeros in the high wave numbers of the spectral domain. The first step of this scheme is to introduce $\frac{N}{2}$ zeros in between the highest positive and negative wave numbers for a set of N Fourier series terms³ for the two quantities whose convolution is being sought. The additional zeros do not introduce any extra information but increase the sampling rate of the Fourier transform. The second step involves the inverse Fourier transform of the spectral amplitudes in the extended Fourier space to the extended physical space. Third step is the multiplication in extended physical space. The fourth step involves the forward transformation of multiplied quantity in physical space back to spectral space. The last step also involves the removal of zero-padded portion to get the dealiased convoluted Fourier spectral amplitude, $\widehat{\mathcal{NL}_\kappa}$. Sharp variations or discontinuities at the points $\frac{N}{2}$ and N introduce spectral leakage at low values of ν (for high Re cases). This leakage creates a localized effect near to the high gradient region in the physical space seen as high frequency ripples. Again no cosmetic smoothing or filtering is performed in our study.

³ Note that we have used the formulation in which the Fourier spectral amplitudes are for the range $0 \leq \kappa < N$. The Discrete Fourier Transform of a real signal is symmetric about 0 and periodic with N .

3.4. 2/3 Truncation & circular truncation scheme

The popular dealiasing scheme, 2/3 Truncation⁴ uses the idea of removing alias prone Fourier modes beyond the region $|\kappa| \geq \frac{N}{3}$ [9,35]. A Fourier window function, also known as Fourier kernel $\mathcal{W}(\kappa)$ is used to remove the high frequency Fourier components. The filtered velocity field $\tilde{u}(x, t)$ and its derivative is expressed as

$$\mathcal{P}_N \{\tilde{u}(x_j)\} = \sum_{\kappa=-\frac{N}{2}+1}^{\frac{N}{2}} \mathcal{W}(\kappa) \hat{u}_\kappa e^{i\kappa x_j}; \frac{d}{dx} \{\mathcal{P}_N \tilde{u}(x_j)\} = i \sum_{\kappa=-\frac{N}{2}+1}^{\frac{N}{2}} \kappa \mathcal{W}(\kappa) \hat{u}_\kappa e^{i\kappa x_j} \quad (36)$$

The one dimensional Fourier window function $\mathcal{W}(\kappa)$ for 2/3 Truncation is

$$\mathcal{W}(\kappa) = \begin{cases} 0, & \text{if } |\kappa| \geq \frac{1}{3}N \\ 1, & \text{otherwise} \end{cases}$$

For example the nonlinear term when using the 2/3 Truncation in VBE in Fourier space can be written as $\mathcal{F}_\kappa \left\{ \tilde{u}(x_j) \frac{d\tilde{u}(x_j)}{dx} \right\}$. The 2/3 Truncation which was expressed as a multiplication of Fourier kernel $\mathcal{W}(\kappa)$ in the Fourier space can also be thought as a one-dimensional Fourier kernel, particularly a box filter in the Fourier space. The kernel of a box filter for 2D Circular Truncation is defined by:

$$\mathcal{W}(\kappa_1, \kappa_2) = \begin{cases} 0, & \text{if } \kappa_1^2 + \kappa_2^2 \geq \left(\frac{\sqrt{2}}{3}N\right)^2 \\ 1, & \text{otherwise} \end{cases}$$

The filtered 2D velocity field is defined in terms of sharp kernel as

$$\tilde{u}(x_i, y_j) = \sum_{|\kappa_1| \leq \frac{N_1}{2}} \sum_{|\kappa_2| \leq \frac{N_2}{2}} \mathcal{W}(\kappa_1, \kappa_2) \hat{u}(\kappa_1, \kappa_2) e^{i(\kappa_1 x_i + \kappa_2 y_j)}$$

The sub-steps of RK2 with the implementation of the Circular Truncation dealiasing scheme are

$$k_1 = \Delta t [\mathcal{W}(\kappa_1, \kappa_2) \otimes \widehat{\mathcal{NL}} \{\hat{u}(\kappa_1, \kappa_2, t^n)\}] + \Delta t \cdot \widehat{\mathcal{V}} \{\hat{u}(\kappa_1, \kappa_2, t^n)\} \quad (37)$$

$$k_2 = \Delta t [\mathcal{W}(\kappa_1, \kappa_2) \otimes \widehat{\mathcal{NL}} \{\hat{u}(\kappa_1, \kappa_2, t^n) + k_1, t_n + \Delta t\}] + \Delta t \cdot \widehat{\mathcal{V}} \{\hat{u}(\kappa_1, \kappa_2, t^n) + k_1, t_n + \Delta t\} \quad (38)$$

It should be noted that although removal of high Fourier modes reduces the overall aliasing errors, the scheme's convergence is affected due to the sudden discontinuity of the box filter in the spectral space resulting in Gibbs oscillations/ripples occurring in the whole physical domain. In this study, we neither apply any cosmetic filter to reduce the Gibbs oscillations nor apply Fourier smoothing windowing function to reduce physical space oscillation and artifacts.

4. Time integration scheme

The governing equations in all three cases⁵ can be written in the form

$$\frac{d\hat{u}(\bar{\kappa}, t)}{dt} = \mathcal{L}[\hat{u}(\bar{\kappa}, t)] \quad (39)$$

where $\mathcal{L}[\hat{u}(\bar{\kappa}, t)]$ represents the right hand side of convection diffusion type equations and $\bar{\kappa} = \kappa_1 \hat{e}_1 + \kappa_2 \hat{e}_2$. $\mathcal{L}[\hat{u}(\bar{\kappa}, t)]$ contains the nonlinear and viscous terms and the nonlinear term is computed using Pseudo-spectral method.

$$\mathcal{L}[\hat{u}(\bar{\kappa}, t)] = -\widehat{\mathcal{NL}}_{\bar{\kappa}} - \nu \kappa^2 \hat{u}(\bar{\kappa}, t) \quad (40)$$

⁴ Sometimes 3/2 Padding is called 2/3 Truncation (see Ref. [4]). The 2/3 Truncation and its higher dimensional analogues (Circular & Spherical Truncation) are essentially different. We differentiate between padding with zeros increasing the number of Fourier amplitude and truncating the existing Fourier series.

⁵ In the case of two dimensional simulation both \hat{u}_1 and \hat{u}_2 need to be advanced in time for all wave numbers (κ_1, κ_2) whereas in the case of one dimensional simulation only wavenumber κ_1 and \hat{u}_1 need to be considered.

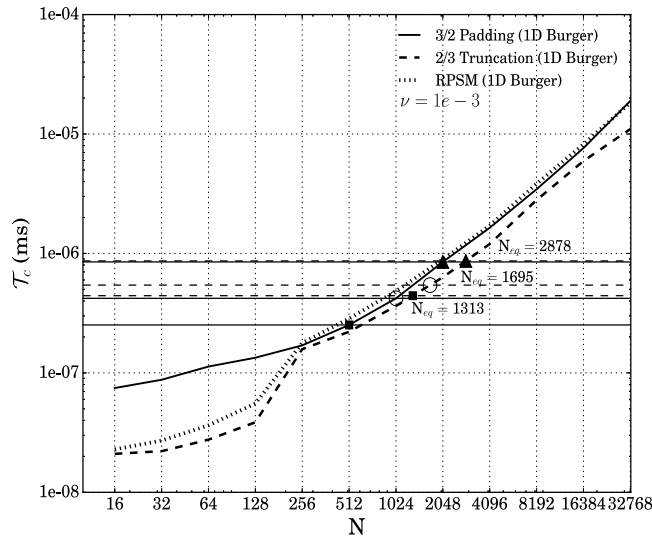


Fig. 3. Computational Time (\mathcal{T}_c) of various dealiasing schemes as a function of spatial resolution (N) for 1D VBE at $v = 1e-3$. Computational time (\mathcal{T}_c) of 3/2 Padding at the spatial resolutions: N = 512, 1024 and 2048 are denoted by the symbols (■), (○) and (▲), respectively. At same values of L_∞ error norm, the corresponding spatial resolutions for 2/3 Truncation scheme called the equivalent spatial resolutions (N_{eq}) are denoted by the same symbols.

Eq. (39) is an initial value problem in spectral space which is marched in time using the so-called low storage second order Runge–Kutta RK2 time integration scheme. The RK2 method is

$$k_1 = \Delta t \mathcal{L}[\hat{u}(\bar{\kappa}, t^n)] \quad (41a)$$

$$k_2 = \Delta t \mathcal{L}[\hat{u}(\bar{\kappa}, t'') + \alpha_1 k_1, t_n + \alpha_2 \Delta t] \quad (41b)$$

and

$$\hat{u}(\bar{\kappa}, t^{n+1}) = \hat{u}(\bar{\kappa}, t^n) + \phi_1 k_1 + \phi_2 k_2 \quad (42)$$

where $\alpha_1, \alpha_2, \phi_1, \phi_2$ are parameters of the RK2 scheme and here we use the classical values, $\alpha_1, \alpha_2 = 1; \phi_1, \phi_2 = \frac{1}{2}$. The appropriate time step for a given viscosity is found in the following way. The advective and viscous timescales for the VBE problem are defined as $\tau_{adv} \equiv \frac{L/N}{U}$ and $\tau_{vis} \equiv \frac{(\Delta x)^2}{6v}$ where $L & U$ are characteristic length and velocity scale of the given problem. Here we choose, $L = 2\pi$ and $U = 1$. Also, Δx is the grid-spacing corresponding to chosen value of N and L with $\Delta x = L/N$ and v is the kinematic viscosity. The smaller of the two time-scales is chosen for advancing the simulation with CFL number set as 0.1, i.e., $\Delta t = (CFL)\min(\tau_{adv}, \tau_{vis})$. For the other two cases, Δt is as per previous studies [48,51].

5. Computational performance of dealiasing schemes

The computational cost and accuracies of the simulations using various dealiasing schemes are markedly different. Before we discuss in detail the simulation results, we first attempt to benchmark the three dealiasing schemes in term of their real-world computational cost. Two benchmarking studies are done, a one-dimensional simulation and the second one is a two-dimensional simulation. For the 1D study, the serial version of the 1D VBE simulation is run on a single processor core of a Fujitsu (Primergy CX 400 S2) server node equipped with Dual Intel Corporation Xeon E7 V2 Processor with 4 GB DDR3-RAM per core. For each value N simulated and a particular dealiasing scheme, the simulation was run for a large number of iterations (about 1×10^6), and the simulation repeated a number of times to obtain averages of simulation running time.

The average value of time taken per iteration for running the 1D VBE simulation at $v = 1e-3$ is reported in Fig. 3. For low values of N, RPSM and 2/3 Truncation based simulations are about 3 times faster than the

Table 1

Computational efficiencies (η_c), equivalent spatial resolution (N_{eq}) of RPSM and 2/3 Truncation Dealiasing schemes in 1D VBE for three different constant values of the L_∞ error norms at $T = 0.5$. The average computational time (\mathcal{T}_c) is in millisecond. The notation $a(-b)$ denotes $a \times 10^{-b}$.

Symbol	3/2 Padding		RPSM			2/3 Truncation			Value of error norm in u	Type of norm
	N	\mathcal{T}_c	N_{eq}	\mathcal{T}_c	η_c	N_{eq}	\mathcal{T}_c	η_c		
■	512	2.52(−7)	345	2.18(−7)	1.16(+0)	1313	4.43(−7)	5.69(−1)	1.41(−1)	L_∞
○	1024	4.21(−7)	940	4.53(−7)	9.29(−1)	1695	5.43(−7)	7.75(−1)	6.95(−2)	L_∞
▲	2048	8.49(−7)	2085	8.89(−7)	9.55(−1)	2878	8.66(−7)	9.80(−1)	9.40(−3)	L_∞

Table 2

Computational efficiencies (η_c) and equivalent spatial resolution (N_{eq}) of CT Dealiasing scheme in 2D shear layer for the different values of the error norms at $t = 4.095$. The average computational time (\mathcal{T}_c) is in millisecond. The notation $a(-b)$ denotes $a \times 10^{-b}$.

Symbol	3/2 Padding		RPSM			CT			Value of error norm in ω	Type of norm
	N	\mathcal{T}_c	N_{eq}	\mathcal{T}_c	η_c	N_{eq}	\mathcal{T}_c	η_c		
■	16	1.56(−6)	18	7.47(−7)	2.09(+0)	89	8.13(−6)	1.92(−1)	1.36(+0)	L_∞
○	16	1.56(−6)	—	—	—	46	2.35(−6)	6.64(−1)	4.79(−1)	L_2
▲	32	3.54(−6)	35	2.11(−6)	1.68(+0)	127	1.85(−5)	1.91(−1)	1.79(−1)	L_2

3/2 Padding based simulation. After $N = 128$ we conclude that the combination of serial FFTW algorithm and the computer architecture creates a bottleneck, as evidenced in Fig. 3, where all the three types of dealiasing schemes based simulations take almost the same time. Multiplication of the complex exponential term becomes computationally expensive for the RPSM scheme in the case of 1D Burgers' equation at higher spatial resolution. We define the term computational efficiency (η_c) as the ratio of time taken for the 3/2 Padding per iteration to the computational time taken for other dealiasing schemes at the same value of error norm (L_2 or L_∞) for the physical quantity considered. Larger values of η_c mean better efficiency. We also introduce the concept of equivalent spatial resolution (N_{eq}) which denotes the equivalent spatial resolution for the 2/3 Truncation (or CT scheme) and RPSM to obtain the same accuracy level of the 3/2 Padding scheme.

From Table 1, we obtain gains in the computational time per iteration ($\Delta\mathcal{T}_c$) for 3/2 Padding scheme 1.9(−7), 1.22(−7) than 2/3 Truncation in the case of 1D VBE at the fixed values of L_∞ error when the corresponding spatial resolutions are $N = 512$ and 1024, respectively. It can be seen that RPSM scheme is computationally more efficient ($\eta_c = 1.16$) than 3/2 Padding in the case of under-resolved simulation ($N = 512$) of 1D VBE at $\nu = 1e-3$. The equivalent spatial resolutions for the 1D 2/3 Truncation scheme are 1313, 1695 & 2878, respectively denoted by the symbols (■), (○) and (▲) at the same values of the L_∞ error norm. It is observed that 2/3 Truncation performs quite better when we select the spatial resolution ($N = 2048$) showing higher computational efficiency ($\eta_c = 0.98$) than that of RPSM ($\eta_c = 0.955$) at $\nu = 1e-3$. The 2/3 Truncation scheme shows similar accuracy as RPSM and 3/2 Padding schemes when the spatial resolution ($N \geq 2048$) is selected at the given kinematic viscosity $\nu = 1e-3$.

Using similar analysis, the N_{eq} for CT scheme at same accuracy level is also shown for 2D Euler equations in Fig. 4 and Table 2. From Table 2, it shows that the η_c of CT scheme is affected due to insufficient spatial resolution to resolve very thin shear layer structures ($\rho = \frac{\pi}{15}$) formed at $t = 4.095$. Computational gains in time per iteration ($\Delta\mathcal{T}_c$) for two dimensional 3/2 Padding scheme are 7.9(−7), 1.5(−5) and 6.57(−6), obtained at the fixed values of L_2 error ($N = 16$), L_2 error ($N = 32$) and L_∞ error ($N = 16$). The 2D computational time vs. spatial resolution plot (Fig. 4) shows that 3/2 Padding scheme is 2.5 times and 2 times more expensive than the CT and RPSM schemes in computational time, respectively. From Fig. 4 and Table 2, same values of the difference in L_2 norm of error for 3/2 Padding of 16–32, 32–64 grids are equivalent to the difference in error norms of grid sizes 46–92 and 127–254 of CT scheme denoted by the symbols (○) and (▲), respectively. For the same value of the difference in L_∞ error norm for 16–32 grid is same as of CT scheme for grid size 89–178 shown by the symbol (■). Computational efficiency study for the SQG flows is not shown for brevity and is similar to the shear layer case.

In both 1D & 2D cases tested, RPSM maintains an intermediate computational cost, between that of 3/2 Padding and 2/3 Truncation. We find that the RPSM is slightly more computationally expensive than 2/3 Truncation yet its accuracy is as good as 3/2 Padding (will be shown in detail in the subsequent section) for the cases tested. In the

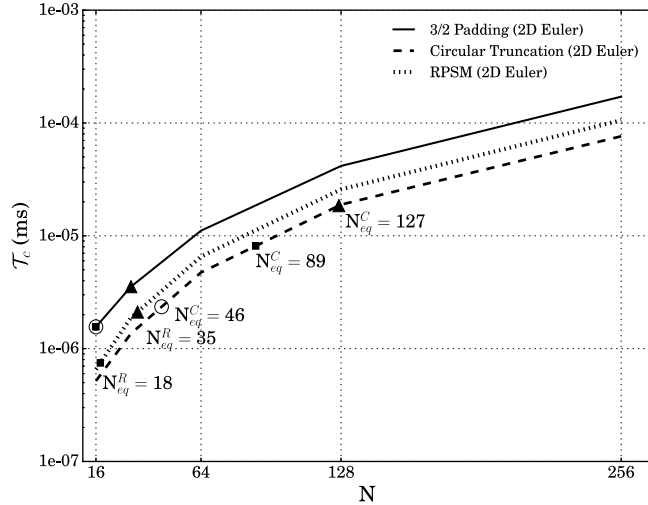


Fig. 4. Computational Time (T_c) of dealiasing schemes as function of Spatial Resolution (N) for 2D Euler equations.

case of 1D VBE once the bottle neck is removed via implementation of parallel codes, it is expected that the same performance gain across the entire range of N can be obtained. This is left for future study and is not in the scope of the present work.

6. Results

In this section, we have presented the validation of the in-house developed codes. Next, we have studied the effect of various dealiasing schemes on three test problems: the VBE equation, 2D shear layers and SQG flows. We evaluate the accuracy of different dealiasing schemes in terms of L_1 , L_2 and L_∞ error norms at different spatial resolutions. The effect of spatial resolution and the occurrence of parasitic currents are emphasized in the present study.

6.1. Validation of the numerical schemes

Burgers' equation displays some similarities with the Homogeneous Isotropic Turbulence (HIT) because it produces multiple scales with time progression. From Fig. 2(a) and (c), the temporal evolution of kinetic energy (k) follows $k \sim T^{-2}$ as predicted at $v = 1e-3$ and $1e-4$ for the VBE. Fig. 2(b) and (d) show that the results obtained from the 1D VBE equation also satisfy the conservation of energy: $\frac{dk}{dt} = -\varepsilon$ which implies the dissipation decays as $\varepsilon \sim T^{-3}$. Next, we validate our in-house Pseudo-spectral based incompressible NS solver implemented with the RK2 based RPSM, CT and 3/2 Padding dealiasing schemes. Results obtained from the different dealiasing schemes will also be compared with the classical Taylor-Green (TG) vortex flow problem [47]. The most commonly used analytical solutions of the decaying 2D incompressible TG vortex flows are as follows [47]:

$$u(x, y, t) = -e^{-2k^2 vt} \cos(kx) \sin(ky) \quad (43a)$$

$$v(x, y, t) = e^{-2k^2 vt} \sin(kx) \cos(ky) \quad (43b)$$

$$p(x, y, t) = -\frac{1}{4}e^{-4k^2 vt} [\cos(2kx) + \cos(2ky)] \quad (43c)$$

where $k = 4$.

Two dimensional incompressible NS equations are simulated in the computational domain, $x, y \in [0, 2\pi] \times [0, 2\pi]$ at $v = 0.0001$ using $N = 512$ and $\Delta t = 1e-4$. The set of initial conditions are taken as

$$u(x, y, 0) = -\cos(kx) \sin(ky); v(x, y, 0) = \sin(kx) \cos(ky); p(x, y, 0) = -\frac{1}{4} [\cos(2kx) + \cos(2ky)] \quad (44)$$

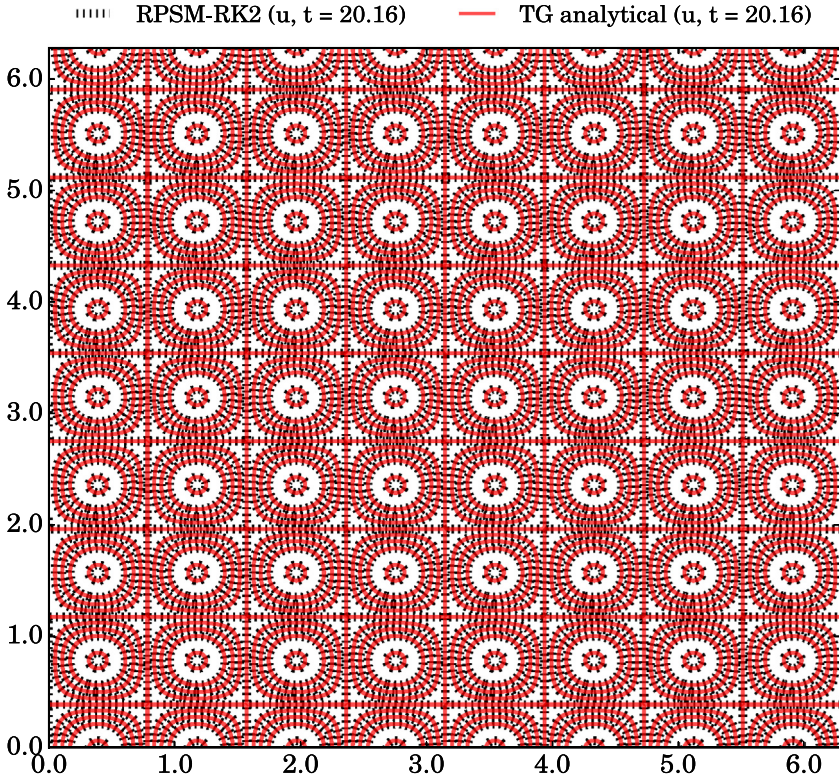


Fig. 5. The velocity component u contours of 2D TG flow problem is compared with the analytical solution at $t = 20.16$.

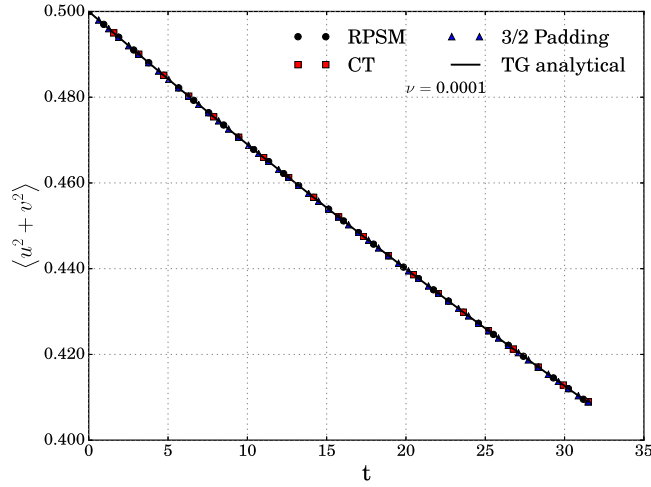


Fig. 6. Temporal evolution of $\langle u^2 + v^2 \rangle$ for 2D TG flows at $\nu = 0.0001$ using $N = 512^2$ grid points.

Fig. 5 shows that the u component of velocity field contours obtained from the TG analytical solution agree well with our numerical result at $t = 20.16$. **Fig. 6** shows that the evolution of $\langle u^2 + v^2 \rangle$ agrees well at $\nu = 0.0001$ for all dealiasing schemes. We validate the results obtained from the SQG flows by comparing the quantity maximum

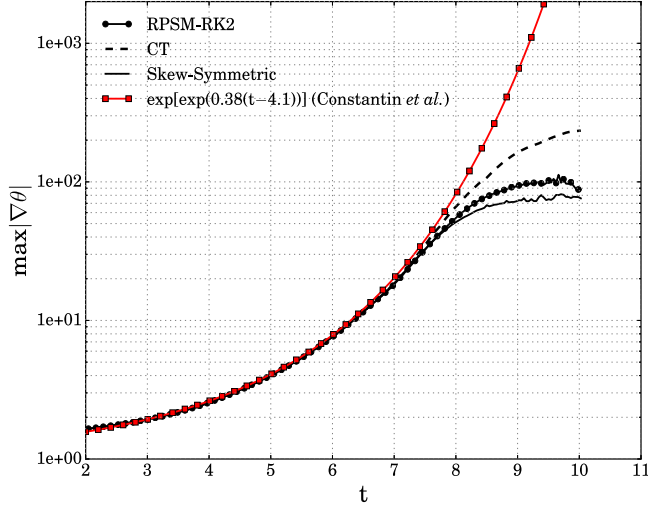


Fig. 7. Variation of $\max |\nabla \theta|$ with time for the SQG flows.

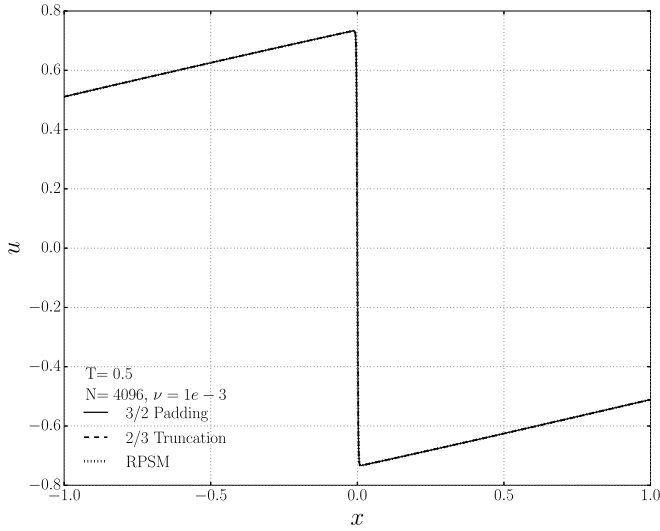


Fig. 8. Velocity u in the region $x \in [-1.0, 1.0]$ for $N= 4096$ & $\nu = 1e-3$ at $T = 0.5$.

of absolute gradient in potential temperature ($\max |\nabla \theta|$) with Constantin et al. [12]. We use similar initial condition of the potential temperature field [12] to compare our results as

$$\theta(x, y, 0) = \sin(x) \sin(y) + \cos(y) \quad (45)$$

From Fig. 7, the evolution of $\max |\nabla \theta|$ agrees well with the double exponential growth predicted as $\exp[\exp(0.38(t - 4.1))]$ in Constantin et al. [12]. The inherent dissipative nature of the RPSM scheme is also visible in $\max |\nabla \theta|$ at later time (see Fig. 7).

6.2. Effect of dealiasing on strong shock in VBE

In the well-resolved set of calculations with $\nu = 1e-3$ and $N = 4096$, strong shock forms at around $T = 0.5$ (see Fig. 8). Note the agreement of all the three methods of calculations at non dimensional time $T = 0.5$. At the

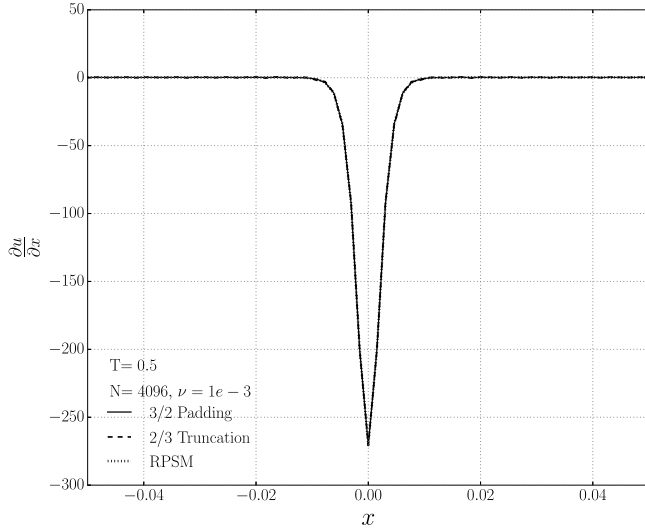


Fig. 9. Velocity gradient $\frac{\partial u}{\partial x}$ in the region $x \in [-0.05, 0.05]$ for $N = 4096$ & $\nu = 1e-3$ at $T = 0.5$.

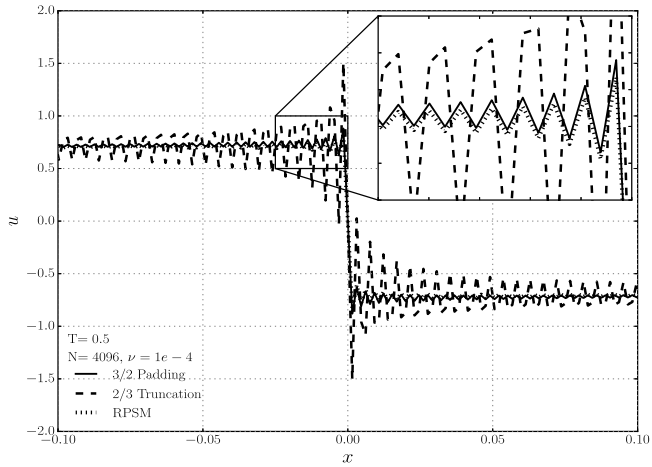


Fig. 10. Velocity u in the region $x \in [-0.1, 0.1]$ for $N = 4096$ & $\nu = 1e-4$ at $T = 0.5$.

time of occurrence of the strong shock, the derivative of $u(x, t)$, $\frac{\partial u}{\partial x}$ (Fig. 9) exhibits a rapid change from a nominal value of zero to a highly negative value at around $x = 0$. This is adequately captured by any of the three methods. However, when we increase the Reynolds number, *i.e.*, decrease the kinematic viscosity to $\nu = 1e-4$, the spectral resolution becomes inadequate even with $N = 4096$. The strong shock that develops around $T = 0.5$ triggers Gibbs phenomena in all three dealiasing methods (Fig. 10). The Pseudo-spectral calculation without use of any dealiasing scheme (not shown) is highly unstable in nature and it blows up in finite time for almost any Reynolds number. In the case of 2/3 Truncation very large oscillations Fig. 10 (dotted line) are noticeable due to the sharp spectral filter cut-off at the wave number $\kappa_c = \frac{N}{3} (\simeq 1365)$ with Gibbs oscillations contaminating the entire solution domain. The effect of oscillation is even more evident in the plot of $\frac{\partial u}{\partial x}$, Fig. 11. Mild oscillations are present in 3/2 Padding scheme due to the windowing effect introduced by zero padding as well as RPSM due to physical space windowing effect. From the insets of Figs. 10 and 11, RPSM shows the oscillations of slightly lesser amplitude in the velocity field and the velocity gradient due to the inherent smoothing effect. The strength of the standing shock formed at $x = 0$ begins to dissipate at later times (nominally $T > 1$). From Fig. 12(c), (d), the effect of Gibbs oscillations is also reduced at later times.

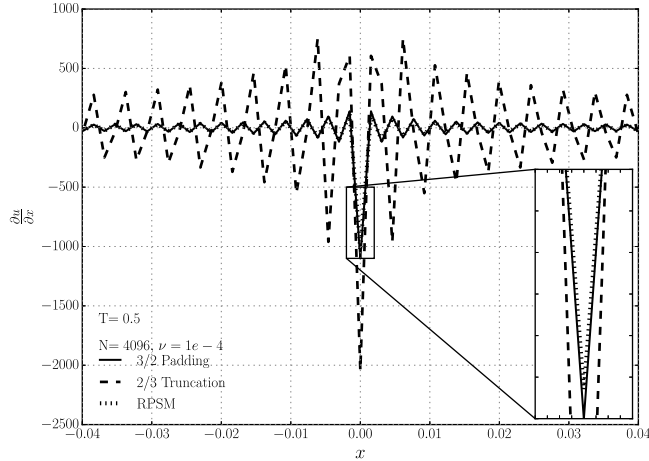


Fig. 11. Velocity gradient $\frac{\partial u}{\partial x}$ in the region $x \in [-0.04, 0.04]$ for $N=4096$ & $\nu = 1e-4$ at $T = 0.5$.

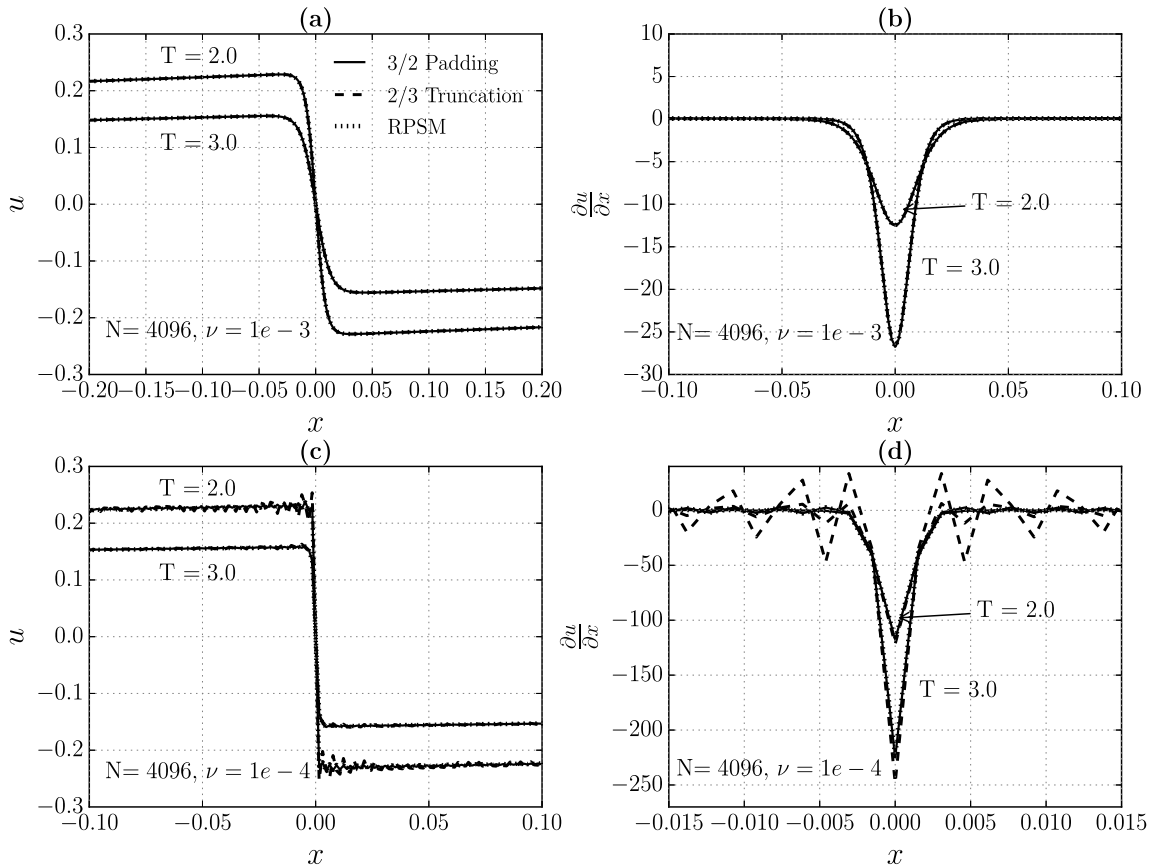


Fig. 12. For $N=4096$ & $\nu = 1e-3$ (a) velocity field u in the region $x \in [-0.2, 0.2]$ (b) velocity gradient $\frac{\partial u}{\partial x}$ in the region $x \in [-0.1, 0.1]$ at $T = 2, 3$; For $N= 4096$ & $\nu = 1e-4$ (c) velocity field u in the region $x \in [-0.1, 0.1]$ (d) velocity gradient $\frac{\partial u}{\partial x}$ in the region $x \in [-0.015, 0.015]$ at $T = 2, 3$.

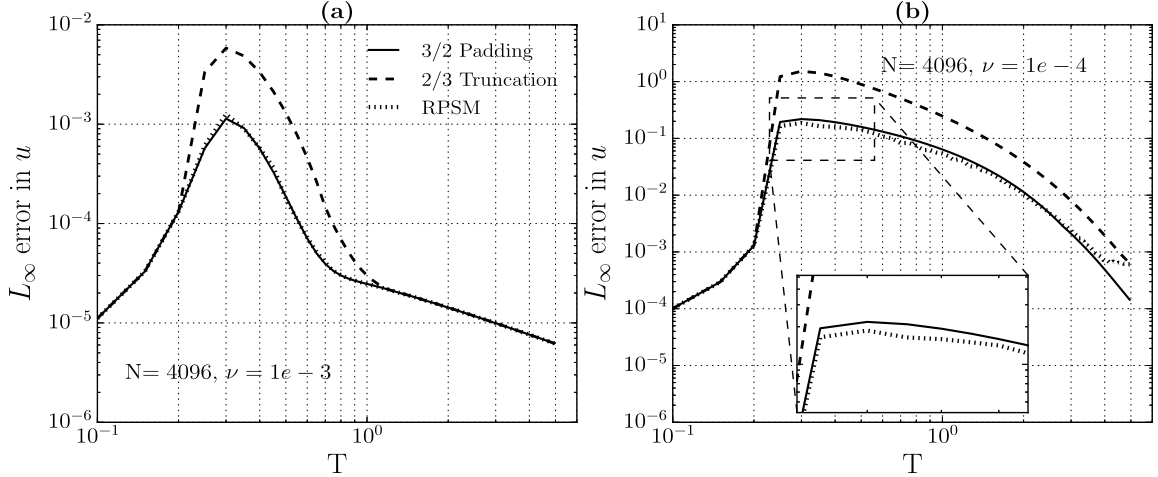


Fig. 13. The temporal evolution of L_∞ norm of errors in the velocity field for $N=4096$ at (a) $\nu = 1e-3$ (b) $\nu = 1e-4$.

We use the error norms L_1 , L_2 and L_∞ [16,44] & [45] to quantify the accuracy of various dealiasing schemes. For a 1D problem they are defined as follows:

$$L_1 = \frac{1}{N} \sum_{i=0}^{N-1} |f(x_i, t^n) - \tilde{f}(x_i, t^n)| \quad (46)$$

$$L_2 = \frac{1}{\sqrt{N}} \sqrt{\sum_{i=0}^{N-1} |f(x_i, t^n) - \tilde{f}(x_i, t^n)|^2} \quad (47)$$

$$L_\infty = \max(|f(x_i, t^n) - \tilde{f}(x_i, t^n)|) \quad (48)$$

where $\tilde{f}(\cdot)$ denotes the reference high resolution Pseudo-spectral solutions using fully dealiased 3/2 Padding scheme. The spatial resolutions $N = 16\,384$ and $N = 32\,768$ are taken as oscillation free reference solutions for $\nu = 1e-3$ & $1e-4$, respectively. The error norms are calculated for various spatial resolutions: $N = 1024, 2048, 4096$ and 8192 summarized in Table 3. From Table 3, it can be observed that the RPSM scheme works quite well for the under-resolved simulations during the formation of strong shock, *i.e.*, almost as good as the fully dealiased 3/2 Padding for a given N . It is also remarkable that the magnitude of L_∞ errors of RPSM for under-resolved simulations are lesser than any other schemes at $T = 0.5$. The inherent smoothing property of RPSM helps to suppress the oscillations produced in under-resolved spectral simulations. As the RPSM scheme removes the aliasing errors partially, the overall accuracy (L_2 & L_∞ errors) of RPSM is lesser than the 3/2 Padding at later time. The error norms at later times ($T = 2.0, 3.0$) shows the reduced accuracy (from Table 3) of RPSM compared to 3/2 Padding at later time. The error norms also indicate that RPSM performs markedly better than 2/3 Truncation. Fig. 13(a), (b) show that the L_∞ error norms for the flow quantities $u(x)$ for the case of higher kinematic viscosity, $\nu = 1e-3$ and for the case of lower viscosity $\nu = 1e-4$, respectively. From Fig. 13, the salient consistent feature to be observed is that for both viscosities the 2/3 Truncation method results in higher error norms consistent with earlier observations. From the inset of Fig. 13(b), it is noticed that RPSM scheme performs even better than 3/2 Padding in under resolved 1D VBE velocity field (u) at $\nu = 1e-4$ due to its inherent filtering ability. In Fig. 14 the convergence in terms of L_2 & L_∞ errors are shown as a function of resolution (N) at the time of formation of strong shock ($T = 0.5$). From Fig. 14(a), (b), we observe that the accuracy of the 2/3 Truncation scheme is less at $T = 0.5$. From Fig. 14(a), the slopes of the L_2 error in u vs. N plot indicate that all the three dealiasing schemes have nearly same convergence rates. From 14(b), it is observed that the convergence of 2/3 Truncation scheme is slightly lesser when the L_∞ errors are considered. Fig. 14(c) and (d) indicate that the convergence rate is quite high for 3/2 padding scheme between the resolutions ($N = 1024, 2048$). It is also seen that the RPSM scheme shows better accuracy but poor convergence at $T = 0.5$. Fig. 14(c) shows that $N = 1024$ of 3/2 Padding scheme shows

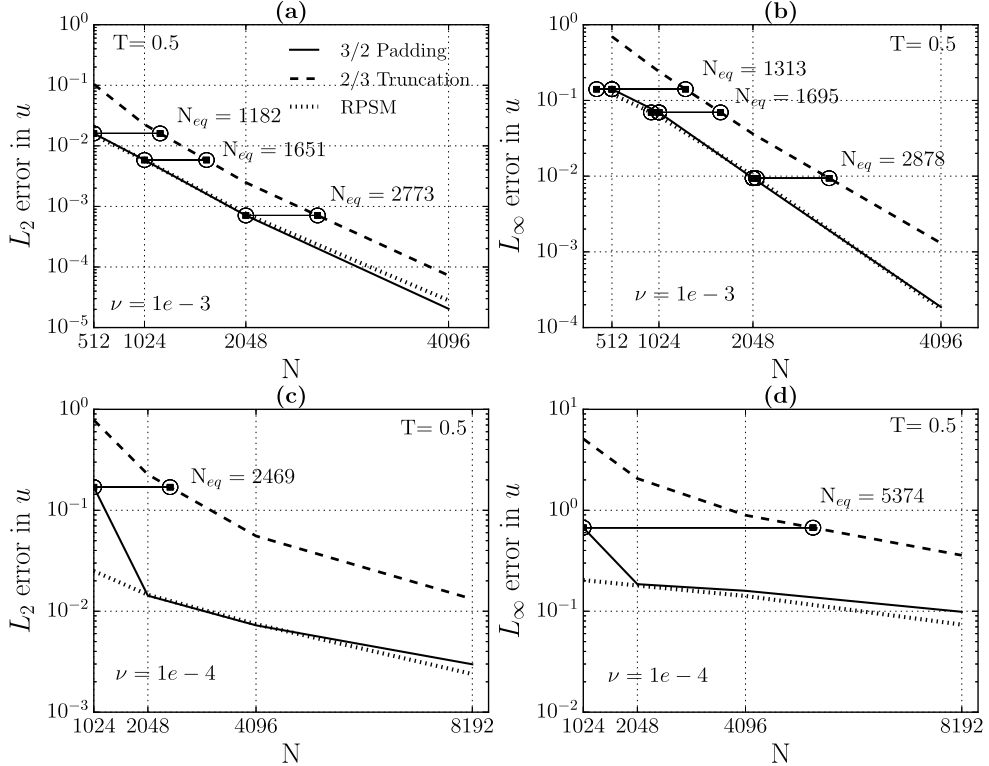


Fig. 14. For $\nu = 1e-3$, variation of (a) L_2 (b) L_∞ norm of errors with N at $T = 0.5$; For $\nu = 1e-4$, variation of (c) L_2 (d) L_∞ norm of errors with N at $T = 0.5$. The equivalent spatial resolutions (N_{eq}) for 2/3 Truncation have been shown at the constant error norms with 3/2 Padding in (a), (b), (c) and (d).

same accuracy as $N_{eq} = 2496$ of 2/3 Truncation in terms of L_2 error norm in u at $\nu = 1e-4$ and the value of N_{eq} is 5374 considering the L_∞ error norm (shown in Fig. 14(d)). Significant deviations in accuracy and convergence are observed in all the cases of dealiasing schemes in both short and late times. From Fig. 15(a), slight decrement in the rate of convergence of RPSM is observed when the resolution exceeds 2048. Similar behavior is also noticed in Fig. 16(a) at $T = 3.0$. From Figs. 15(b) and 16(b), L_∞ norm of errors in u shows that all dealiasing schemes perform nearly similar at $N = 4096$ and later times $T = 2.0, 3.0$ but the L_2 error in u shows slightly higher value at $N = 4096$. Fig. 16(c) and (d) show that the convergence rates of the RPSM scheme are affected when the spatial resolution N exceeds the value 2048. Considering the L_∞ error norm, the corresponding spatial resolutions (N_{eq}) of RPSM are 1652, 1837 for $N = 2048$ of 3/2 Padding at $T = 2.0$ and 3.0 , respectively. It indicates the better computational performance of RPSM at the time of development of strong shock. From Fig. 16(c), convergence of u in terms of L_2 error norms that same accuracy is obtained for all the three dealiasing schemes for $N = 8192$, $\nu = 1e-4$ at $T = 3.0$.

6.3. Effects of dealiasing in shear layer problem

The unstable shear layer governed by the Inviscid Euler equations is simulated using the Fourier Pseudo-spectral method using the three dealiasing schemes as described in Section 2.2, Eq. (9) and others. The three dealiasing schemes are contrasted using coarse spatial resolutions ($N = 32, 64, 128 \& 256$) and the time step size $\Delta t = 0.001$. From Fig. 17, it is seen that the thick shear layer ($\rho = \pi/15$) gradually evolves into thinner structures. RPSM scheme displays its capability to resolve the fine scale roll up structures quite accurately even with the coarse grid ($N = 128$). Fig. 17(h) shows the detrimental effect of spurious oscillations formed at $t = 5.355$ in the thick shear layer problem ($\rho = \pi/15$) for the CT scheme. This problem is even more severe in the case of the thin shear layer problem ($\rho = \pi/150$), Fig. 19. It can be observed that the popular Circular Truncation (CT) scheme is incapable

Table 3

Comparison of L_1 , L_2 and L_∞ errors in velocity field (u) for the 1D Viscous Burgers' equation given by 3/2 Padding, 2/3 Truncation and RPSM schemes at ($\nu = 1e-4$). The notation $a(-b)$ denotes $a \times 10^{-b}$.

N	3/2 Padding			2/3 Truncation			RPSM		
	L_1	L_2	L_∞	L_1	L_2	L_∞	L_1	L_2	L_∞
N = 1024 (T = 0.5)	7.11(-2)	1.69(-1)	6.72(-1)	5.48(-1)	7.84(-1)	5.10(+0)	1.79(-2)	2.50(-2)	2.03(-1)
N = 1024 (T = 2.0)	1.07(-1)	1.11(-1)	4.59(-1)	2.30(-1)	2.92(-1)	2.39(+0)	8.20(-3)	9.18(-3)	4.68(-2)
N = 1024 (T = 3.0)	5.60(-2)	5.93(-2)	2.90(-1)	1.88(-1)	2.16(-1)	1.27(+0)	5.42(-3)	6.06(-3)	2.73(-2)
N = 2048 (T = 0.5)	8.85(-3)	1.43(-2)	1.85(-1)	1.42(-1)	2.26(-1)	2.06(+0)	8.70(-3)	1.45(-2)	1.80(-1)
N = 2048 (T = 2.0)	1.16(-3)	2.20(-3)	3.55(-2)	6.86(-2)	7.65(-2)	1.43(-1)	2.59(-3)	3.29(-3)	2.98(-2)
N = 2048 (T = 3.0)	6.68(-4)	1.04(-3)	1.51(-2)	3.91(-2)	4.38(-2)	1.89(-1)	1.48(-3)	1.76(-3)	1.30(-2)
N = 4096 (T = 0.5)	2.85(-3)	7.25(-3)	1.59(-1)	2.94(-2)	5.56(-2)	8.93(-1)	3.03(-3)	7.44(-3)	1.41(-1)
N = 4096 (T = 2.0)	1.57(-4)	5.15(-4)	1.13(-2)	6.77(-4)	1.81(-3)	3.83(-2)	3.45(-4)	6.16(-4)	1.04(-2)
N = 4096 (T = 3.0)	3.60(-5)	1.13(-4)	2.09(-3)	1.94(-4)	4.05(-4)	7.97(-3)	1.55(-4)	2.05(-4)	2.43(-3)
N = 8192 (T = 0.5)	8.38(-4)	2.98(-3)	9.87(-2)	5.30(-3)	1.32(-2)	3.58(-1)	7.23(-4)	2.39(-3)	7.36(-2)
N = 8192 (T = 2.0)	2.72(-5)	4.20(-5)	8.06(-4)	3.77(-5)	1.25(-4)	3.10(-3)	3.46(-5)	5.00(-5)	9.05(-4)
N = 8192 (T = 3.0)	1.76(-5)	2.04(-5)	7.89(-5)	1.59(-5)	2.12(-5)	2.68(-4)	2.02(-5)	2.36(-5)	1.11(-4)

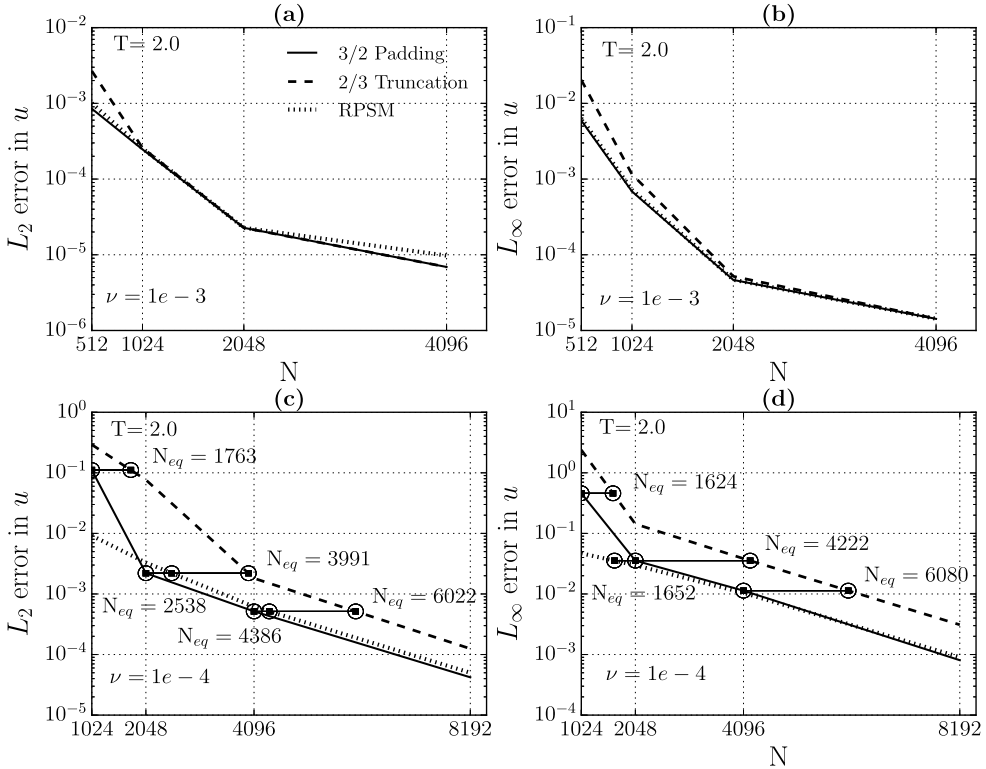


Fig. 15. For $\nu = 1e-3$, variation of (a) L_2 (b) L_∞ norm of errors with N at $T = 2.0$; For $\nu = 1e-4$, variation of (c) L_2 (d) L_∞ norm of errors with N at $T = 2.0$. The equivalent spatial resolutions (N_{eq}) for 2/3 Truncation have been shown at the constant error norms with 3/2 Padding in (c), (d).

of resolving the very thin roll up structures accurately, while the RPSM scheme performs nearly as well as 3/2 Padding. These unphysical spurious fine scale structures are observed in the vorticity field (ω) when the traditional CT scheme is used (Fig. 19). Accurate and efficient solutions can be obtained for under-resolved shear layer by using the RPSM dealiasing scheme without resorting to the computationally expensive 3/2 Padding scheme. We have used Richardson extrapolation between two grid sizes (e.g. 32–64) to quantify the accuracy of the various

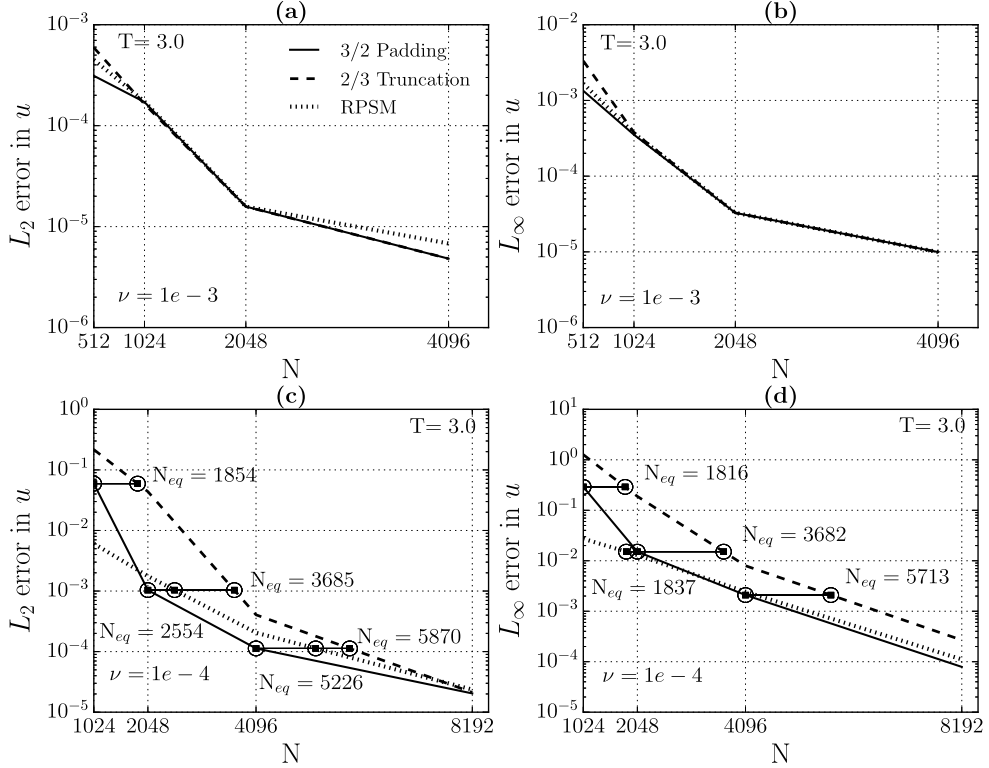


Fig. 16. For $\nu = 1e-3$, variation of (a) L_2 (b) L_∞ norm of errors with N at $T = 3.0$; For $\nu = 1e-4$, variation of (c) L_2 (d) L_∞ norm of errors with N at $T = 3.0$. The equivalent spatial resolutions (N_{eq}) for 2/3 Truncation have been shown at the constant error norms with 3/2 Padding.

dealiasing schemes. The error norms for the 2D cases are calculated using,

$$L_1 = \frac{1}{N^2} \sum_{i=0}^{N-1} \sum_{j=0}^{N-1} |f^{(\Delta x)}(x_i, y_j, t^n) - f^{(2\Delta x)}(x_i, y_j, t^n)| \quad (49)$$

$$L_2 = \frac{1}{N} \sqrt{\sum_{i=0}^{N-1} \sum_{j=0}^{N-1} |f^{(\Delta x)}(x_i, y_j, t^n) - f^{(2\Delta x)}(x_i, y_j, t^n)|^2} \quad (50)$$

$$L_\infty = \max(|f^{(\Delta x)}(x_i, y_j, t^n) - f^{(2\Delta x)}(x_i, y_j, t^n)|) \quad (51)$$

Here $f^{(\Delta x)}(\cdot)$ and $f^{(2\Delta x)}(\cdot)$ denote the numerical results in finer and coarser grids, respectively. The RPSM scheme shows satisfactory accuracy in double shear layer roll up problem in which small scale structures are formed due to KH instability. From the values of L_1 , L_2 and L_∞ in Table 4 show that the RPSM scheme has similar spatial convergence as the 3/2 Padding while the CT suffers poor spectral convergence especially at $t = 2.20$ & 2.52 . As the thinner structures gradually evolve in time, it is also observed that the values of the error norms grow in time. So, the performance of RPSM for under resolved thin shear layer problem is quite promising for both small scale quantities that involve gradients (ω) and large scale quantities (u). Fig. 18(a) shows that at the same values of L_2 error norm, spatial resolutions $N = 16, 32$ of 3/2 Padding Scheme are equivalent to 41 and 77 of CT scheme when $t = 1.575$. From Fig. 18(b), CT scheme suffers more at later time ($t = 4.095$) showing $N_{eq} = 46,127$ for CT scheme against $N = 16, 32$ for 3/2 Padding scheme. Fig. 18(d) indicates that $N = 16$ of 3/2 Padding shows same L_∞ error norm as $N = 127$ of CT scheme at $t = 4.095$. The computational efficiency advantages of dealiasing schemes have already been discussed in Section 5.

Table 4

Comparison of L_1 , L_2 and L_∞ errors in vorticity field (ω) for the 2D Euler equations ($\rho = \frac{\pi}{15}$) given by 3/2 Padding, CT and RPSM schemes. Errors are calculated using the Richardson Extrapolation between two grid sizes. The notation $a(-b)$ denotes $a \times 10^{-b}$.

N	3/2 Padding			CT			RPSM		
	L_1	L_2	L_∞	L_1	L_2	L_∞	L_1	L_2	L_∞
(32 – 64) ($t = 1.575$)	2.68(–2)	3.84(–2)	1.73(–1)	6.54(–2)	7.56(–2)	1.34(–1)	2.99(–2)	3.87(–2)	1.67(–1)
(32 – 64) ($t = 4.095$)	1.09(–1)	1.79(–1)	7.11(–1)	4.79(–1)	6.11(–1)	1.78(+0)	1.25(–1)	1.89(–1)	7.53(–1)
(32 – 64) ($t = 5.355$)	1.93(–1)	2.97(–1)	1.01(+0)	6.34(–1)	7.75(–1)	2.15(+0)	1.83(–1)	2.82(–1)	1.06(+0)
(64 – 128) ($t = 1.575$)	1.99(–3)	3.07(–3)	1.70(–2)	6.31(–3)	7.62(–3)	1.71(–2)	2.18(–3)	3.09(–3)	1.46(–2)
(64 – 128) ($t = 4.095$)	6.50(–2)	1.10(–1)	5.25(–1)	2.48(–1)	3.53(–1)	1.65(+0)	7.07(–2)	1.08(–1)	5.41(–1)
(64 – 128) ($t = 5.355$)	1.18(–1)	1.87(–1)	8.70(–1)	6.66(–1)	8.56(–1)	4.18(+0)	1.23(–1)	1.78(–1)	7.91(–1)
(128 – 256) ($t = 1.575$)	1.94(–5)	3.06(–5)	1.81(–4)	7.02(–5)	8.67(–5)	2.84(–4)	2.15(–5)	2.99(–5)	1.61(–4)
(128 – 256) ($t = 4.095$)	2.96(–2)	5.33(–2)	2.86(–1)	1.30(–1)	1.77(–1)	1.02(+0)	3.08(–2)	5.23(–2)	2.73(–1)
(128 – 256) ($t = 5.355$)	6.08(–2)	1.00(–1)	5.30(–1)	3.68(–1)	4.78(–1)	2.07(+0)	6.49(–2)	1.00(–1)	5.02(–1)

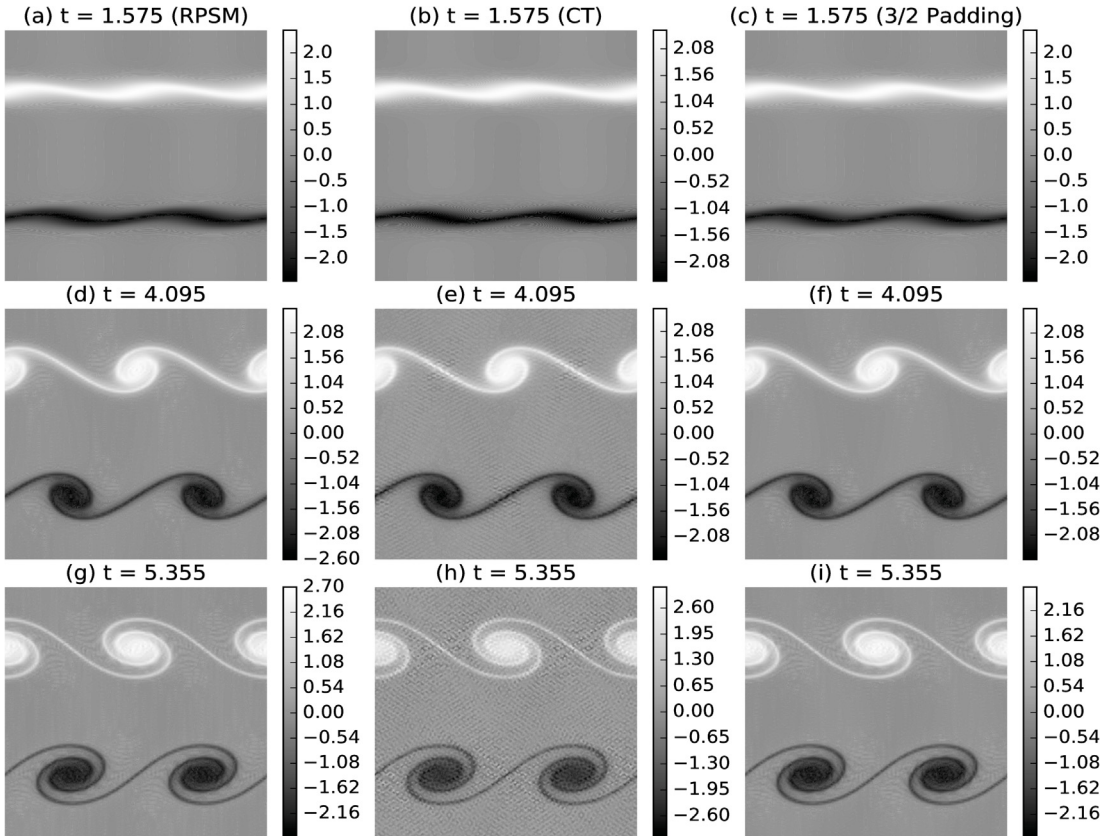


Fig. 17. Vorticity field for (9) with $\rho = \pi/15$, $\Delta t = 0.001$ and $N = 128$.

6.4. Effect of dealiasing in SQG flows

We have implemented the RK2 based RPSM, CT and Skew-symmetric based schemes for simulating the SQG flows. We have used a computational domain, $x, y \in [0, 2\pi] \times [0, 2\pi]$, time step size $\Delta t = 1e-4$ and a fixed spatial resolution $N = 512$. From Fig. 20, it is observed that very thin regions between the positive and negative potential temperature fields (θ) are gradually developed at $t = 4.01$ and 5.61 . It is also noticed that the RK2 based RPSM scheme and the Skew-symmetric form based nonlinear terms are capable of resolving these strong fronts of θ at

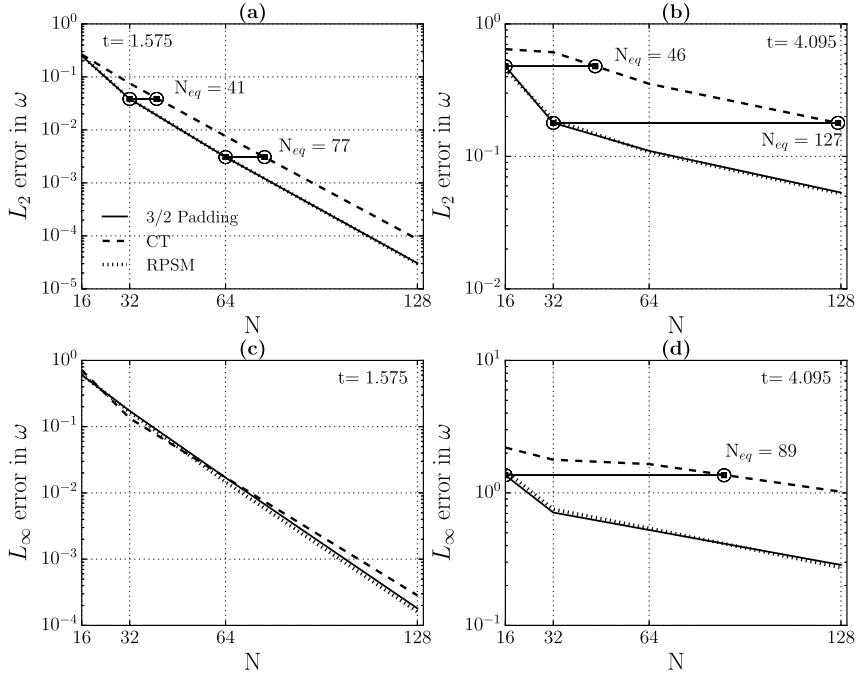


Fig. 18. Variations of L_2 error norms at (a) $t = 1.575$ (b) $t = 4.095$ with N ; variations of L_∞ error norms at (c) $t = 1.575$ (d) $t = 4.095$ with N . The equivalent spatial resolutions (N_{eq}) for CT have been shown at the constant error norms with 3/2 Padding.

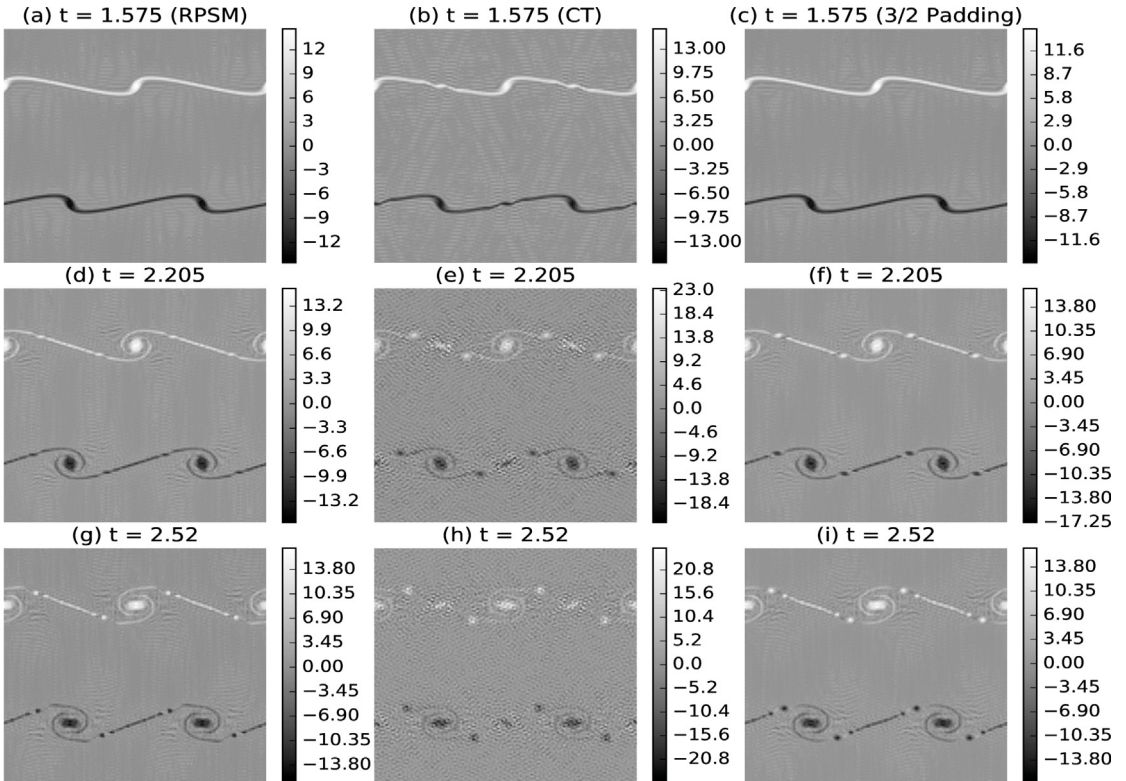


Fig. 19. Vorticity field for (9) with $\rho = \pi/150$, $\Delta t = 0.001$ and $N = 128$.

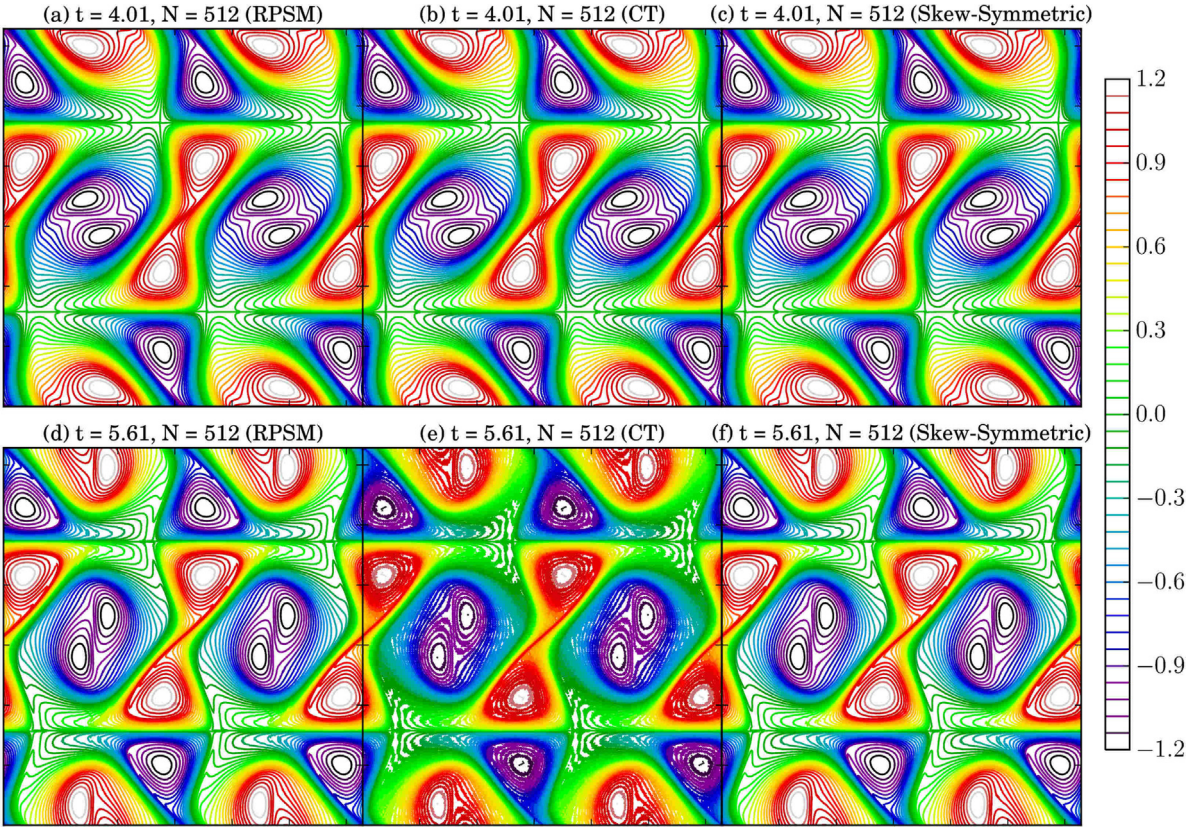


Fig. 20. The potential temperature (θ) contours for the RK2 based RPSM, CT and Skew-symmetric based schemes at $t = 4.01$ and 5.61 .

$t = 4.01$ and 5.61 with significant accuracy using $N = 512$. Due to the formation of spurious oscillatory structures, filtering based schemes blow up quickly but we have not noticed blow-up of the RK2 based RPSM scheme. The effect of the residual aliasing error of the RK2 based RPSM scheme may be responsible for these smooth potential field contours.

7. Conclusions

Here in the present study, we have investigated RPSM dealiasing scheme and contrasted with the popular 2/3 Truncation scheme and the accurate 3/2 Padding scheme for the DNS of flows with strong gradients. It is observed that the correct choice of dealiasing is important for the fixed spatial resolution problems. The DNS is performed using Fourier collocation in the tradition of Orszag [38] and Rogallo [42] using the Pseudo-spectral scheme. For the case of strong shock, the DNS of VBE simulations with two kinematic viscosities $\nu = 1e-3$ and $\nu = 1e-4$ are performed with the number of collocation points set at $N = 4096$, thus resulting in adequately resolved simulation for the higher kinematic viscosity and under resolved simulation for the lower kinematic viscosity. This has been done to simulate prevalent trend of traditional DNS where the higher Reynolds numbers are attempted with a given size of N sometime resulting in slight under resolution of the far dissipation scales. Inviscid simulations are also carried out for the 2D double shear layer problem with the shear layer parameter $\rho = \frac{\pi}{15}, \frac{\pi}{150}$ using the three dealiasing schemes. The SQG flows are also simulated using the RK2 based RPSM, CT, higher order exponential smoothing spectral filter and skew-symmetric form of the nonlinear term.

In section 5, performance of dealiasing schemes is studied in terms of computational time (T_c) and efficiency (η_c). It is found that RPSM is more efficient than 2/3 Truncation for a given accuracy of the computation in case of 1D viscous Burgers' equation (VBE) at $\nu = 1e-3$. In Section 6.2, we have explained the velocity evolution of various dealiasing schemes work similar at $\nu = 1e-3$ but the effect of Gibbs phenomena becomes very strong in

the case of 2/3 Truncation at $\nu = 1e-4$ resulting in violent oscillations throughout the domain. Lesser oscillations are observed in 3/2 Padding and RPSM due to zero padding and physical space discontinuity, respectively. 2/3 Truncation performs the worst as its deviation of damping ratio from unity is maximum. In Section 6.3, we observe more spurious vortices present in the vorticity field simulated using CT scheme. We have also found that the RK2 based RPSM scheme shows better convergence in terms of different error norms.

In conclusion, we find the Random Phase Shift Method [42] is superior in capturing the details of a nearly singular solution in the DNS of the viscous Burgers' Equation without too high a computational accuracy penalty compared with the popular and computationally efficient 2/3 Truncation scheme. The vortices in the thin shear layer are captured correctly by the RPSM scheme in the 2D Euler equations. It is also observed that lesser spurious structures are present in the solution of 2D Euler equations. RPSM is found to be nearly as accurate as the fully dealiased 3/2 Padding scheme for the under resolved simulations. It also shows superior accuracy in under resolved 2D shear layer problem. We find the 2/3 Truncation scheme although satisfactory for some aspects of resolving the nearly singular solution in the DNS of the VBE in a well-resolved simulation velocity and vorticity field in 2D shear layer are all inaccurately captured. For an under resolved simulation, 2/3 Truncation method becomes unusable whereas the RPSM still maintains a good deal of fidelity. The work is being extended to include other RK schemes. More work is required to look into the dissipative effect of RPSM and the effects of intrinsic filtering.

Acknowledgments

The authors would like to gratefully acknowledge IIT Bhubaneswar, India and the Institute Seed, India Grant SP 0042 for the generous support. The authors would like to thank P.K. Yeung, Matthew Clay, Anirban Bhattacharya and Yogesh G. Bhumkar for their many suggestions and help in preparing the manuscript. The authors would also like to thank the reviewer for helpful comments.

References

- [1] C. Basdevant, M. Deville, P. Haldenwang, J. Lacroix, J. Ouazzani, R. Peyret, P. Orlandi, A. Patera, Spectral and finite difference solutions of the Burgers equation, *Comput. Fluids* 14 (1) (1986) 23–41, [http://dx.doi.org/10.1016/0045-7930\(86\)90036-8](http://dx.doi.org/10.1016/0045-7930(86)90036-8).
- [2] J.B. Bell, P. Colella, H.M. Glaz, A second-order projection method for the incompressible Navier-Stokes equations, *J. Comput. Phys.* 85 (2) (1989) 257–283, [http://dx.doi.org/10.1016/0021-9991\(89\)90151-4](http://dx.doi.org/10.1016/0021-9991(89)90151-4).
- [3] G. Boffetta, A. Mazzino, S. Musacchio, L. Vozella, Statistics of mixing in three-dimensional Rayleigh–Taylor turbulence at low Atwood number and Prandtl number one, *Phys. Fluids* 22 (3) (2010) 035109, <http://dx.doi.org/10.1063/1.3371712>.
- [4] J.P. Boyd, *Chebyshev and Fourier Spectral Methods*, Courier Corporation, 2001.
- [5] D.L. Brown, Performance of under-resolved two-dimensional incompressible flow simulations, *J. Comput. Phys.* 122 (1) (1995) 165–183, [http://dx.doi.org/10.1016/S0021-9991\(03\)00206-7](http://dx.doi.org/10.1016/S0021-9991(03)00206-7).
- [6] K.A. Brucker, J.C. Isaza, T. Vaithianathan, L.R. Collins, Efficient algorithm for simulating homogeneous turbulent shear flow without remeshing, *J. Comput. Phys.* 225 (1) (2007) 20–32, <http://dx.doi.org/10.1016/j.jcp.2006.10.018>.
- [7] Q.-D. Cai, S. Chen, A memory-saving algorithm for spectral method of three-dimensional homogeneous isotropic turbulence, *Commun. Comput. Phys.* 9 (5) (2011) 1152–1164, <http://dx.doi.org/10.4208/cicp.191209.111110s>.
- [8] C. Canuto, M. Hussaini, A. Quarteroni, T.A. Zang, *Spectral Methods Fundamentals in Single Domains*, Springer, 2006, <http://dx.doi.org/10.1007/978-3-540-30726-6>.
- [9] C.G. Canuto, M.Y. Hussaini, A.M. Quarteroni, T.A. Zang, *Spectral Methods: Evolution to Complex Geometries and Applications to Fluid Dynamics (Scientific Computation)*, Springer-Verlag New York, Inc., 2007, <http://dx.doi.org/10.1007/978-3-540-30728-0>.
- [10] M. Clay, D. Buaría, T. Gotoh, P. Yeung, A dual communicator and dual grid-resolution algorithm for petascale simulations of turbulent mixing at high Schmidt number, *Comput. Phys. Comm.* 219 (2017) 313–328, <http://dx.doi.org/10.1016/j.cpc.2017.06.009>.
- [11] P. Constantin, M.-C. Lai, R. Sharma, Y.-H. Tseng, J. Wu, New numerical results for the surface quasi-geostrophic equation, *J. Sci. Comput.* 50 (1) (2012) 1–28, <http://dx.doi.org/10.1007/s10915-011-9471-9>.
- [12] P. Constantin, Q. Nie, N. Schörghofer, Nonsingular surface quasi-geostrophic flow, *Phys. Lett. A* 241 (3) (1998) 168–172, [http://dx.doi.org/10.1016/S0375-9601\(98\)00108-X](http://dx.doi.org/10.1016/S0375-9601(98)00108-X).
- [13] S. Derevyanko, The $(n+1)/2$ rule for dealiasing in the split-step Fourier methods for n -wave interactions, *IEEE Photonics Technol. Lett.* 20 (23) (2008) 1929–1931, <http://dx.doi.org/10.1109/LPT.2008.2005420>.
- [14] M. Frigo, S.G. Johnson, FFTW: an adaptive software architecture for the FFT, in: *Acoustics, Speech and Signal Processing, 1998. Proceedings of the 1998 IEEE International Conference on*, Vol. 3, IEEE, 1998, pp. 1381–1384, <http://dx.doi.org/10.1109/ICASSP.1998.681704>.
- [15] M. Frigo, S.G. Johnson, *FFTW: Fastest Fourier transform in the west*, *Astrophys. Source Code Libr.* 1 (2012) 1201.015.
- [16] E. Garnier, P. Sagaut, M. Deville, A class of explicit ENO filters with application to unsteady flows, *J. Comput. Phys.* 170 (1) (2001) 184–204, <http://dx.doi.org/10.1006/jcph.2001.6732>.

- [17] T. Gotoh, S. Hatanaka, H. Miura, Spectral compact difference hybrid computation of passive scalar in isotropic turbulence, *J. Comput. Phys.* 231 (21) (2012) 7398–7414, <http://dx.doi.org/10.1016/j.jcp.2012.07.010>.
- [18] R. Grauer, C. Marliani, K. Germaschewski, Adaptive mesh refinement for singular solutions of the incompressible Euler equations, *Phys. Rev. Lett.* 80 (19) (1998) 4177, <http://dx.doi.org/10.1103/PhysRevLett.80.4177>.
- [19] Y. Gu, Y. Zhou, G. Wei, Conjugate filters with spectral-like resolution for 2D incompressible flows, *Comput. & Fluids* 32 (6) (2003) 777–794, [http://dx.doi.org/10.1016/S0045-7930\(02\)00066-X](http://dx.doi.org/10.1016/S0045-7930(02)00066-X).
- [20] P. Gualtieri, C. Casciola, R. Benzi, G. Amati, R. Piva, Scaling laws and intermittency in homogeneous shear flow, *Phys. Fluids* 14 (2) (2002) 583–596, <http://dx.doi.org/10.1063/1.1427919>.
- [21] H. Homann, J. Dreher, R. Grauer, Impact of the floating-point precision and interpolation scheme on the results of DNS of turbulence by pseudo-spectral codes, *Comput. Phys. Comm.* 177 (7) (2007) 560–565, <http://dx.doi.org/10.1016/j.cpc.2007.05.019>.
- [22] T.Y. Hou, R. Li, Computing nearly singular solutions using pseudo-spectral methods, *J. Comput. Phys.* 226 (1) (2007) 379–397, <http://dx.doi.org/10.1016/j.jcp.2007.04.014>.
- [23] T.Y. Hou, R. Li, Blowup or no blowup? the interplay between theory and numerics, *Physica D* 237 (14) (2008) 1937–1944, <http://dx.doi.org/10.1016/j.physd.2008.01.018>.
- [24] Z. Hu, C.L. Morfey, N.D. Sandham, Sound radiation in turbulent channel flows, *J. Fluid Mech.* 475 (2003) 269–302, <http://dx.doi.org/10.1017/S002211200200277X>.
- [25] T.J. Hughes, L. Mazzei, A.A. Oberai, A.A. Wray, The multiscale formulation of large eddy simulation: Decay of homogeneous isotropic turbulence, *Phys. Fluids* 13 (2) (2001) 505–512, <http://dx.doi.org/10.1063/1.1332391>.
- [26] M. Iovieno, C. Cavazzoni, D. Tordella, A new technique for a parallel dealiased pseudospectral Navier–Stokes code, *Comput. Phys. Comm.* 141 (3) (2001) 365–374, [http://dx.doi.org/10.1016/S0010-4655\(01\)00433-7](http://dx.doi.org/10.1016/S0010-4655(01)00433-7).
- [27] P.J. Ireland, L.R. Collins, Direct numerical simulation of inertial particle entrainment in a shearless mixing layer, *J. Fluid Mech.* 704 (2012) 301–332, <http://dx.doi.org/10.1017/jfm.2012.241>.
- [28] P.J. Ireland, T. Vaithianathan, P.S. Sukheswalla, B. Ray, L.R. Collins, Highly parallel particle-laden flow solver for turbulence research, *Comput. & Fluids* 76 (2013) 170–177, <http://dx.doi.org/10.1016/j.compfluid.2013.01.020>.
- [29] Y. Kaneda, T. Ishihara, K. Gotoh, Taylor expansions in powers of time of Lagrangian and Eulerian two-point two-time velocity correlations in turbulence, *Phys. Fluids* 11 (8) (1999) 2154–2166, <http://dx.doi.org/10.1063/1.870077>.
- [30] D. Kopriva, *Implementing Spectral Methods for Partial Differential Equations: Algorithms for Scientists and Engineers*, Springer Science & Business Media, 2009.
- [31] P. Mininni, A. Pouquet, Helicity cascades in rotating turbulence, *Phys. Rev. E* 79 (2) (2009) 026304, <http://dx.doi.org/10.1103/PhysRevE.79.026304>.
- [32] P. Mininni, A. Pouquet, D. Montgomery, Small-scale structures in three-dimensional magnetohydrodynamic turbulence, *Phys. Rev. Lett.* 97 (24) (2006) 244503, <http://dx.doi.org/10.1103/PhysRevLett.97.244503>.
- [33] M.L. Minion, D.L. Brown, Performance of under-resolved two-dimensional incompressible flow simulations, II, *J. Comput. Phys.* 138 (2) (1997) 734–765, [http://dx.doi.org/10.1016/S0021-9991\(03\)00206-7](http://dx.doi.org/10.1016/S0021-9991(03)00206-7).
- [34] M. Mortensen, H.P. Langtangen, High performance Python for direct numerical simulations of turbulent flows, *Comput. Phys. Comm.* 203 (2016) 53–65, <http://dx.doi.org/10.1016/j.cpc.2016.02.005>.
- [35] S.A. Orszag, Numerical methods for the simulation of turbulence, *Phys. Fluids* (1958–1988) 12 (12) (1969) II–250, <http://dx.doi.org/10.1063/1.1692445>.
- [36] S.A. Orszag, On the elimination of aliasing in finite-difference schemes by filtering high-wavenumber components, *J. Atmos. Sci.* 28 (6) (1971) 1074, [http://dx.doi.org/10.1175/1520-0469\(1971\)028<1074:OTEAOI>2.0.CO;2](http://dx.doi.org/10.1175/1520-0469(1971)028<1074:OTEAOI>2.0.CO;2).
- [37] R. Ostilla-Monico, Y. Yang, E.P. van der Poel, D. Lohse, R. Verzicco, A multiple-resolution strategy for direct numerical simulation of scalar turbulence, *J. Comput. Phys.* 301 (2015) 308–321, <http://dx.doi.org/10.1016/j.jcp.2015.08.031>.
- [38] G. Patterson Jr., S.A. Orszag, Spectral calculations of isotropic turbulence: Efficient removal of aliasing interactions, *Phys. Fluids* (1958–1988) 14 (11) (1971) 2538–2541, <http://dx.doi.org/10.1063/1.1693365>.
- [39] P. Perlekar, D. Mitra, R. Pandit, Manifestations of drag reduction by polymer additives in decaying, homogeneous, isotropic turbulence, *Phys. Rev. Lett.* 97 (26) (2006) 264501, <http://dx.doi.org/10.1103/PhysRevLett.97.264501>.
- [40] S.B. Pope, *Turbulent Flows*, Cambridge University Press, 2000.
- [41] M. Roberts, J.C. Bowman, Dealiased convolutions for pseudospectral simulations, in: *Journal of Physics: Conference Series*, Vol. 318, IOP Publishing, 2011, 072037, <http://dx.doi.org/10.1088/1742-6596/318/7/072037>.
- [42] R.S. Rogallo, *An ILLIAC Program for the Numerical Simulation of Homogeneous Incompressible Turbulence*, Vol. 73203, National Aeronautics and Space Administration, 1977.
- [43] R.S. Rogallo, *Numerical Experiments in Homogeneous Turbulence*, Vol. 81315, National Aeronautics and Space Administration, 1981.
- [44] C.-W. Shu, P.S. Wong, A note on the accuracy of spectral method applied to nonlinear conservation laws, *J. Sci. Comput.* 10 (3) (1995) 357–369, <http://dx.doi.org/10.1088/0951-7715/7/6/001>.
- [45] Y. Sun, Y. Zhou, S.-G. Li, G.W. Wei, A windowed Fourier pseudospectral method for hyperbolic conservation laws, *J. Comput. Phys.* 214 (2) (2006) 466–490, <http://dx.doi.org/10.1016/j.jcp.2005.09.027>.
- [46] M. Tanahashi, S. Iwase, T. Miyachi, Appearance and alignment with strain rate of coherent fine scale eddies in turbulent mixing layer, *J. Turbul.* 2 (6) (2001) 1–18.
- [47] G.I. Taylor, A.E. Green, Mechanism of the production of small eddies from large ones, *Proc. R. Soc. A* 158 (895) (1937) 499–521, <http://dx.doi.org/10.1098/rspa.1937.0036>.

- [48] D. Wan, Y. Zhou, G. Wei, Numerical solution of incompressible flows by discrete singular convolution, *Internat. J. Numer. Methods Fluids* 38 (8) (2002) 789–810, <http://dx.doi.org/10.1002/fld.253>.
- [49] E. Weinan, C.-W. Shu, A numerical resolution study of high order essentially non-oscillatory schemes applied to incompressible flow, *J. Comput. Phys.* 110 (1) (1994) 39–46, <http://dx.doi.org/10.1006/jcph.1994.1004>.
- [50] T.A. Zang, On the rotation and skew-symmetric forms for incompressible flow simulations, *Appl. Numer. Math.* 7 (1) (1991) 27–40, [http://dx.doi.org/10.1016/0168-9274\(91\)90102-6](http://dx.doi.org/10.1016/0168-9274(91)90102-6).
- [51] Y. Zhou, G. Wei, High resolution conjugate filters for the simulation of flows, *J. Comput. Phys.* 189 (1) (2003) 159–179, [http://dx.doi.org/10.1016/S0021-9991\(03\)00206-7](http://dx.doi.org/10.1016/S0021-9991(03)00206-7).